Journal of Molecular Liquids 352 (2022) 118735

Contents lists available at ScienceDirect

Journal of Molecular Liquids

journal homepage: www.elsevier.com/locate/molliq

Adsorption of endocrine disruptive congo red onto biosynthesized silver nanoparticles loaded on *Hildegardia barteri* activated carbon

Kehinde Shola Obayomi [a,b,*], Sie Yon Lau [b], Divine Akubuo-Casmir [a], Muibat Diekola Yahya [c], Manase Auta [c], A.S.M. Fazle Bari [d,e], Ayomide Elizabeth Oluwadiya [a], Oluwatobi Victoria Obayomi [f], Mohammad Mahmudur Rahman [d]

[a] Department of Chemical Engineering, Landmark University, PMB 1001, Omu-Aran, Kwara State, Nigeria
[b] Department of Chemical Engineering, Curtin University, CDT 250, 98009 Miri, Sarawak, Malaysia
[c] Department of Chemical Engineering, School of Infrastructure, Process Engineering and Technology, Federal University of Technology, PMB 65, Minna, Niger State, Nigeria
[d] Global Centre for Environmental Remediation (GCER), College of Engineering, Science and Environment, The University of Newcastle, Callaghan, NSW 2308, Australia
[e] Department of Soil Science, Sher-e-Bangla Agricultural University, Dhaka, Bangladesh
[f] Department of Food Science and Technology, Obafemi Awolowo University, Ile-Ife, Osun State, Nigeria

ARTICLE INFO

Article history:
Received 29 December 2021
Revised 27 January 2022
Accepted 8 February 2022
Available online 12 February 2022

Keywords:
Nano-composite
Response surface methodology
Silver nanoparticles
Antibacterial activity
Dye adsorption
Regeneration

ABSTRACT

In this research work, silver nanoparticles (AgNPs) were prepared using green procedure and loaded on *Hildegardia barteri* activated carbon (HBAC) and then characterized for determination of morphology, crystals structure, functional groups, surface area and porosity, and size distribution, of the composite material using Scanning electron microscope equipped with energy dispersive X-ray spectroscopy (SEM-EDX), X-ray diffraction (XRD), Fourier-transform infrared spectroscopy (FTIR), Brunauer Emmett Teller (BET), and High-resolution transmission electron microscope (HRTEM). The AgNPs/HBAC nanocomposite was used for the removal of Congo red (CR) dye from aqueous solution. The antimicrobial activity of AgNPs/HBAC was tested against *Pseudomonas aeruginosa, Salmonella typhi, Escherichia coli* and *Bacillus subtilis* bacteria using the agar well diffusion method. Parameters such as initial CR concentration (20–100 mg/L), adsorbent dosage (0.1–1 g), contact time (0–90 min), and adsorption temperature (308, 318 and 328 K) were investigated on a batch adsorption process to estimate the CR removal efficiency. The mesoporous AgNPs/HBAC had a BET surface area of 794 m^2/g which enhanced CR adsorption capacity (161.29 mg/g). The Freundlich isotherm emerged the best fitted model, indicating surface heterogeneity (multilayer adsorption) between the CR and AgNPs/HBAC surface. The CR adsorption onto AgNPs/HBAC was adequately described by a pseudo-second order kinetic model, and the overall adsorption process was governed by Webber-Morris intraparticle diffusion, and liquid film diffusion models. Thermodynamic study revealed that the adsorption ability of AgNPs/HBAC toward CR was spontaneous, feasible, and exothermic. The developed AgNPs/HBAC could be used as a nano-adsorbent to mitigate the environmental problems caused by CR in wastewater. Regeneration and reusability of AgNPs/HBAC adsorption performance indicated adsorption efficiency greater than 85 % after five successive cycles.

1. Introduction

Water pollution has become a worldwide concern in recent years because it causes serious threats to human life and ecosystem [1]. Urbanization, industrialization, and population increase are the major primary source of water pollution thus, affecting aquatic life, stability in the environment and lowering the quality of water resources for commercial use [2,3]. Dyes are essential components of many industries including textiles, paint, printing, food, tannery, pharmaceutical, cosmetics, rubber, and photographic industries [4]. These dyes substance when ingested are mutagenic, carcinogenic and highly toxic to aquatic environment and human life due to their resistance to biodegradation under aerobic conditions [5,6]. Dyes, when discharged into water bodies without proper treatment pose a real threat to the aquatic environment by disrupting biological activity, aquatic organisms, water reoxygenation capacity and reduces phytoplankton photosynthetic rate by reducing light penetrability [7].

* Corresponding author at: Department of Chemical Engineering, Landmark University, PMB 1001, Omu-Aran, Kwara State, Nigeria.
E-mail addresses: obayomi.kehinde@lmu.edu.ng, obayomikehindeshola@gmail.com (K.S. Obayomi).

https://doi.org/10.1016/j.molliq.2022.118735
0167-7322/

Congo red (CR, $C_{32}H_{22}N_6Na_2O_6S$) is a common diazo anionic dye which contains two azo groups(–N=N–) bond in its molecular structure with at least one end connected to an aromatic group [4,8]. Due to their mutagenic, carcinogenic, and other toxic properties, CR has been banned in many countries. However, because it adds a bright red color to fabrics, it is still widely used in most industries [9,10]. The toxicity of CR poses potential health risks by causing dizziness, mucous membrane damage, vomiting, diarrhea, genetic mutations, and respiratory irritation and damages the human central nervous system [11]. The quality of water available to a population is directly related to their health and well-being, as well as the socio-economic development of the society, therefore, removing CR dye molecules from industrial wastewater is crucial and has received significant attention to scientific community and environmental regulators [12].

Numerous methods have been used to combat the threat posed by pollutants in wastewater, including reverse osmosis, ion exchange, coagulation and flocculation, membrane separation, photocatalytic degradation, biological degradation, chemical precipitation, electrochemical process, advanced oxidation and adsorption [6,13,8,14]. Among these techniques, adsorption is regarded as one of the well-established techniques for the treatment of pollutants in wastewater as a result of its simplicity of design, low energy requirement, high adsorption efficiency, low cost, easy recovery, eco-friendliness, and ability to adsorb soluble and insoluble organic pollutants [15,16].

Activated carbon (AC), among other adsorbents, is widely used adsorbent for organic and inorganic pollutants removal from wastewater [17]. Agricultural waste materials have recently attracted attention as an alternative to existing commercial materials for activated carbon development due to their thermal and mechanical stability, availability, cost effectiveness, desirable surface area, eco-friendliness, and excellent adsorption ability, [18,19]. Recently, almond tree dry leaves [20], spent tea leaves [21], pineapple leaves [22], mango leaves [23], Dead Ashoka leaves [24], *Aloe vera* waste leaves [25], *Albizia procera* leaves [26] and *Acalypha indica* leaves [27], have been studied and reported for the development of AC and utilized to remove organic and inorganic pollutants.

Nanomaterials most especially metal nanoparticles have received a great deal of attention from the scientific community owing to their mechanical strength, high surface volume ratio, metallic or semi-metallic behavior, electrical and thermal conductivity, chemical stability, and ease of synthesis with distinct crystallinity and controllable structure [28,29]. Metal nanoparticle synthesis via physical and chemical methods has drawbacks such as toxic byproduct generation, high energy consumption, and high cost. As a result of the need for an alternative technique capable of overcoming these drawbacks, a new field of research on green and environmentally friendly methods has emerged [30].

Green plant resources, which are free of chemical toxicity and provide natural capping agents, provide a better platform for silver nanoparticles (AgNPs) [31]. Furthermore, the use of plant resources reduces the cost of microorganism isolation and culture media, improving the cost-competitive feasibility of microorganism nanoparticle synthesis [32]. Plants have unique phytochemicals and metabolites that help them develop AgNPs faster and more efficiently than microbes [33]. Plant phytochemicals aid in the capping of AgNPs, which results in stable and dispersed AgNPs. [34]. AgNPs are being considered for use as an adsorbent for pollutant treatment due to their high surface area at the nanometer scale [35]. Several studies have recently reported antimicrobial, antifungal, anticancer, antioxidant, and antiplasmodial activities of AgNPs [36,37,38,33,39]. The AgNPs synthesis using several plant leaf extracts such as *Ocimum tenuiflorum*, *Mentha spicata*, and *Azadirachta indica* [40], *Hagenia abyssinica* [41], *Conocarpus lancifolius* [42], *Piper nigrum*, *Ziziphus spina-christi* and *Eucalyptus globulus* [43], *Cissus quadrangularis* [44], *Citrus medica, Tagetes lemmonii*, and *Tarenna asiatica* [45], *Brillantaisia patula*, *Crossopteryx febrifuga* and *Senna siamea* [46] and *Cassytha filiformis* [32] have been reported in literature.

AC has been utilized in several studies as an adsorbent for CR removal, but few studies have reported the use of AgNPs loaded on AC as an adsorbent, no study to the best of our knowledge has reported the utilization of biosynthesized AgNPs from *Ocimum gratissimum* leaves extract loaded on developed *Hildegardia barteri* leave activated carbon to remove CR from aqueous solution. In this study, process variable optimization using central composite design (CCD), a statistical experimental design technique, an aspect of the response surface methodology (RSM), was used to obtain the optimum conditions for the development of high yield *H. barteri* leave activated carbon and CR removal efficiency prior to loading AgNPs. The influence of CR concentration, adsorbent dosage, contact time and temperature on the adsorbent surface in a batch process adsorption was studied. The adsorption isotherms, kinetics, thermodynamics, regenerability, reusability as well as the antimicrobial activity were also examined.

2. Materials and methods

2.1. Materials and chemicals

O. gratissimum and H. barteri fresh leaves were obtained from Landmark University, Omu-Aran Teaching and Research Farm. Analytical grade chemicals such as Potassium hydroxide (KOH), aqueous silver nitrate ($AgNO_3$), congo red ($C_{32}H_{22}N_6Na_2O_6S_2$), Mueller hinton ager, and dimethyl sulfoxide (DMSO) were procured from Sigma Aldrich.

2.2. Activated carbon preparation

The *H. barteri* leaves employed for the development of AC was collected, washed severally with distilled water to remove dirt and other foreign bodies before being used and dried at 100 °C for 2 h. The dried leaves of *H. barteri* were loaded into a crucible and then carbonized in a muffle furnace with a quartz tubular reactor. The muffle furnace temperature was set to 300 °C and maintained for 30 min at 20 °C/min heating rate using N_2 at a flowrate of 25 mL/min. The char prepared after cooling at room temperature, was then subjected to activation by mixing with KOH solution as activating agent under predetermined impregnation ratio (g KOH/g percussor). The mixture was allowed for 2 h to activate and dried at 108 °C in an oven overnight. The dried impregnated char was then transferred to the furnace for activation under the consideration of the following variables: activation temperature (300–500 °C) and activation time (30–60 min) as specified experimental conditions (**Table S1**). The synthesized *H. barteri* activated carbon (HBAC) was allowed to cool at room temperature before being thoroughly washed with distilled water to attain a neutral pH (6.8–7.0) before being stored in an airtight container for further use.

2.3. Design of experiment (DOE)

CCD was employed to statistically optimize the parameters selected for the HBAC synthesis. The percentage production yield and CR removal are the two responses to this optimization. The interaction between the independent variables and the response variables was determined using ANOVA, and these parameters were also correlated with the response using an empirical model based on the optimal predictive quadratic equation given as

$$y = \beta_o + \sum_{i=1}^{k} \beta_i X_i + \sum_{i=1}^{k} \beta_{ii} X_i^2 + \sum_{i<j} \beta_{ij} X_i X_j \quad (1)$$

where y denotes the predicted response, β_o is the constant of coefficient, $\beta_i, \beta_{ii}, \beta_{ij}$, denotes linear, quadratic and interaction coefficients, Xi, Xj represent the independent variables considered.

Design Expert was employed to fit the equation developed through regression analysis and to assess the significance of the resulting equation. **Table S2** revealed the coded variable levels and their corresponding values**.** The response variable, percentage production yield, was calculated using the equation given as

$$Actiavted\ carbon\ yield\ (Y\%) = \frac{Weight\ of\ dried\ activated\ carbon\ prepared\ (g)}{weight\ of\ dried\ precursor\ (g)} \times 100 \quad (2)$$

Table S1 revealed that Run 12 gave the highest percentage yield and CR removal. Therefore, this study will be based on singular response which is the percentage HBAC yield.

2.4. Development of AgNPs and nanocomposite

2.4.1. Biosynthesis of AgNPs

The hydrothermal method was used to prepare *O. gratissimum* leaf extract. The freshly collected plant material was washed several times with distilled water to remove debris before being oven dried at 70 °C and powdered. 20 g of the dried powdered leaf material was added to 250 mL Erlenmeyer flask containing 100 mL of deionized water and boiled at 80 °C for 45 min on a magnetic stirrer and the solution mixture was allowed to cool (room temperature), filtered through Whatman filter paper No. 40. 10 mL of the filtrated leaf extract was poured into an Erlenmeyer flask (250 mL) and mixed with 90 mL AgNPs (1 mM); the prepared reaction mixture was incubated at 25 °C in the dark for 24 h. Then, the solution had changed colour from yellow to brown, indicating the formation of AgNPs. The reaction was monitored using a UV–Visible spectrophotometer.

2.4.2. AgNPs loaded on H. barteri activated carbon

The synthesis of *O. gratissimum* AgNPs loaded on *H. barteri* activated carbon (AgNPs/HBAC) was conducted using a straight forward agitation method. 5 g of HBAC was measured and added to 50 mL of prepared AgNPs solution in a 250 mL Erlenmeyer flask. The mixture was stirred vigorously using a magnetic stirrer continuously at 140 rpm for 2 h. The mixture was then oven dried at 105 °C for 1 h to obtain the desired nanocomposite adsorbent (AgNPs/HBAC) and was stored properly for further use.

2.5. Characterizations of AgNPs, HBAC and AgNPs/HBAC nanocomposite

The surface morphology together with the elemental compositions were examined using scanning electron microscope (SEM) (Zeiss Sigma, Germany) equipped with a Bruker energy dispersive X-ray spectroscopy (EDX) detector. The materials surface chemistry was investigated using the Fourier-transform infrared (FTIR, Agilent Cary 600) over the range of 4000–400 cm^{-1}. The materials crystallinity structure was examined using the X-ray diffractometer (XRD, Bruker D8 Advance model (Cu - Kα radiation). The diffractogram at room temperature was measured over 2θ = 10 to 80° range with 0.02° step size. The textural properties were examined with Brunauer Emmett Teller (BET, Tristar™ II 3020, Micromeritics, USA). The materials size distribution and shape were investigated using a high-resolution transmission electron microscope (HRTEM, JEM-2100F, Japan). The point of zero charge (pH_{PZC}) of the prepared AgNPs/HBAC was determined using the procedure described by Auta and Hameed [11].

2.6. Congo red adsorption

CR dye stock solution was first freshly prepared by dissolving 1 g powder dye in 1000 mL of distilled water and stirred for 6 h. The stock solution was then stored in dark condition in other to avoid its degradation. The prepared stock solution was used to prepare other smaller concentrations as required. Batch adsorption experiments were carried out in a set of Erlenmeyer flasks (250 mL) containing 100 mL of CR dye solutions at various initial concentrations (20–100 mg/L). To achieve equilibrium, 0.1 g AgNPs/HBAC was added each to the flasks containing the CR solutions, mixed, and placed in a water bath isothermal shaker at a shaker speed of 140 rpm, for 2 h at 35 °C. The water bath shaker temperature was adjusted to 45 and 55 °C respectively, and the procedure was repeated with another set of flasks containing the same but different initial CR concentrations (20–100 mg/L). All experiments were carried out in triplicates. Aliquots were taken at regular time intervals and the final dye concentrations in the solution were analyzed using a UV–Vis double beam spectrophotometer at a maximum wavelength of 497 nm [47]. The removal efficiency and amount of CR adsorbed, at equilibrium q_e (mg/g) was evaluated using the equations.

$$\%MBremoval = \left(\frac{C_o - C_e}{C_o}\right) \times 100 \quad (3)$$

$$q_e = \frac{(C_0 - C_e)V}{W} \quad (4)$$

where C_o and C_e are the initial and equilibrium concentration of CR dye (mg/L) respectively; V is the dye solution volume (L); and W is the weight of the adsorbent used (g). The amount of CR dye adsorbed at a fixed time interval (t), q_t (mg/g) is given by;

$$q_t = \frac{(C_0 - C_t)V}{W} \quad (5)$$

Chi-square (χ^2) statistical error analysis was employed to determine the best fitted isotherm model to the CR adsorption process onto AgNPs/HBAC. Significantly, the isotherm model that best describes the adsorption process must have lower values of χ^2 and higher values of the regression correlation coefficient (R^2) [4]. The χ^2 statistical error analysis equation is given as;

$$\chi 2 = \sum_{i=1}^{n} \frac{(q_{e,calc} - q_{e,meas})^2}{q_{e,meas}} \quad (6)$$

where $q_{e,\ calc}$ and $q_{e,\ meas}$ is the amount of CR dye calculated and measured in mg/g.

2.7. AgNPs/HBAC regenerability and reusability study

A batch adsorption process was used for the regeneration of AgNPs/HBAC. After being used to adsorb CR molecules, the exhaust AgNPs/HBAC was regenerated by washing with ethanol and distilled water several times to ensure the disappearance of the coloured CR on the adsorbent (desorption process) in order to restore the adsorbent material to its original form. After washing, the regenerated AgNPs/HBAC was oven dried at 108 °C for 2 h and transferred into the conical flask containing the CR and the mixture was placed on the shaker at equilibrium conditions. The batch desorption process was studied under optimal conditions, which included contact time of 60 min, adsorbent dosage of 0.4 g, 100 mg/L initial CR concentration and a pH of 2.

3. Results and discussion

3.1. Statistical analysis of developed HBAC

3.1.1. Regression model establishment

The quadratic regression model equation, which is part of the RSM as proposed by the CCD, was employed to investigate the interaction impact of the variables considered on the HBAC percentage yield. In accordance with the design expert's recommendation, 20 experimental runs were conducted. The results of those experiments are shown in **Table S1**. The highest percentage HBAC yield of 62.27 % was attained at Run 12 (impregnation ratio = 1:1; activation temperature = 300 °C; and activation time = 60 min) whereas the lowest yield of 20.56 % was attained at Run 8 (impregnation ratio = 3:1; activation temperature = 500 °C; and activation time 30 min). The relative predictive power of the quadratic model quality which include the R^2 (0.987), adjusted R^2 (0.975) and predicted R^2 (0.886) was observed to be within the desirability range [48]. Thus, the quadratic regression model equation for the HBAC yield response is given by;

$$Y(\%) = 51.20 - 4.02x_1 - 10.09x_2 + 7.79x_3 - 3.87x_1x_2 - 4.05x_1x_3 + 3.17x_2x_3 + 1.07x^1 - 2.52x^2 - 5.44x^3 \quad (7)$$

3.1.2. Analysis of variance (ANOVA)

In order to highlight the model's appropriateness and its impact on the percentage yield of HBAC, an ANOVA was used. The calculated F-values and P-values (prob > F) obtained for the percentage yield, as shown in **Table S3**, clearly revealed that the model was highly significant, and the obtained quadratic regression equation can explain the variation in response. The Model F-value of 83.59 implies that the model is significant, with only a 0.01 % chance that F-value of this large could occur due to noise. The P-values less than 0.0500 indicated that the model terms were significant. In this case x_1, x_2, x_3, x_1x_2, x_1x_3, x_2x_3, x_2^2, x_3^2 are the significant model terms while x_1^2 is the only observed insignificant term. The lack of fit F-value of 4.09 indicates that there is a 7.42 % chance that a large lack of fit F-value could occur due to noise. The quadratic regression model coefficient of variance (C.V) value of 3.69 % confirms the reliability and the mean acceptable variation of the experiment [49]. The percentage yield level of significance can be deduced from the highest sum of square values through the relationship: activation temperature (x_2) > activation time (x_3) > impregnation ratio (x_1. Furthermore, the p-values (<0.05) obtained for these coefficients; linear (x_1, x_2, and x_3), interactive (x_1x_2, x_1x_3, and x_2x_3) and quadratic (x_2^2, and x_3^2) were the significant terms for the percentage yield response [50]. The activation temperature and time were discovered to have the most significant effect on the percentage yield. This conclusion was reached based on their highest F-values of 327.95 and 195.58 obtained through either a single variable approach (x_1, x_2) or interaction between the variables (x_1x_2) **(see Table S3)**. The final quadratic regression equation model in terms of the coded equation, excluding the insignificant terms, is given by equation (8):

$$Y(\%) = 51.20 - 4.02x_1 - 10.09x_2 + 7.79x_3 - 3.87x_1x_2 - 4.05x_1x_3 + 3.17x_2x_3 - 2.52x^2 - 5.44x^3 \quad (8)$$

A negative coefficient has an antagonistic effect on percentage yield, whereas a positive coefficient has a synergistic impact [50]. For determining the suitable power transformation, the Box-Cox plot was a good starting point. According to the plot, a transformation model is recommended if the standard transformation (current lambda (λ)) value obtained is outside of the low- and high-confidence intervals (CI). The Box-Cox plot result indicated that a transformation model was not recommended. This is due to the fact that the current value ($\lambda = 1$) falls within the confidence intervals and is closer to the optimal design values (-0.31 and 1.14) as shown in **Fig. S1 (a)**. The quadratic mathematical model for the percentage yield on HBAC synthesis was further analyzed using the normal plot of residuals and the residual versus run number plot to determine the quadratic model's fitness to the experimental data. The closeness of the data points to the straight line, as shown in **Fig. S1(b)**, indicated that the model residuals are normally distributed, thereby satisfying the analysis's assumption [51,49]. The residuals versus run number plots shown in **Fig. S1(c)** revealed that the data points are distributed randomly around 0 and between externally studentized residuals of −4.15 and +4.15, indicating that at different synthesis variable conditions, all residuals were found to be uncorrelated with one another [52,53]. As a result, the quadratic model is appropriate and effectively describes the interactive impact of the variables considered on the preparation of HBAC surface area.

3.1.3. Response surface 3-dimensional plots

The 3-dimensional surface response plots generated from the selected quadratic regression model were used to examine the interactive effects of impregnation ratio (x_1), activation temperature (x_2), and activation time (x_3) on HBAC percentage yield, as shown in Fig. 1. The plots revealed that the three factors contributed to the percentage yield either individually or through interaction although with different level of contributions. The percentage yield of HBAC obtained revealed that all three variables on the response were significant. Comparison of individual contributions to the response, it was discovered that activation temperature had the greatest contribution with the highest F-value of 327.9. Fig. 1**(a)** depicts the interaction effect of impregnation ratio and activation temperature at zero level activation time (45 min). It is possible to chemically activate carbon at high temperatures with an abundant impregnation ratio because the volatile matter in the precursor is volatilized, consequently releasing some carbon compounds through a series of reactions [54]. According to the plots, impregnation ratio and activation time had the greatest impact on the results, as demonstrated in Fig. 1**(b)**. Moreover, Fig. 1**(c)** demonstrates that activation time and temperature had no effect on the response since only dehydration operations were possible owing to the absence of an activating agent to spark the needed reaction [55]. As shown in the final equation **(Eq.8)**, the impregnation ratio and activation temperature independent variables had a negative influence on yield due to the release of volatile matter, dehydration, and continuous removal of tar from the pores during activation, resulting in greater weight loss. [50].

3.1.4. Process optimization

The primary goal of this study is to identify the best process parameters that can be used to maximize the HBAC percentage yield from the developed quadratic mathematical model equation. In order to maximize the percentage yield, the major parameters considered for HBAC preparation were impregnation ratio, activation temperature, and activation time. To categorize the desirability function of the yield response, Design Expert statistical software was employed. The design process's economic viability was investigated by aiming for the maximum response (yield) while varying the ranges of selected independent parameters. The desirability range function assigns values ranging from 0 to 1, with "0″ representing the most undesirable response and "1″ representing the most desirable or ideal response [56]. As shown in **Table S4**, the high desirability conditions were discovered to be an impregnation ratio of 1.078:1, activation temperature of 306.787, and activation time of 44.502, which were selected and

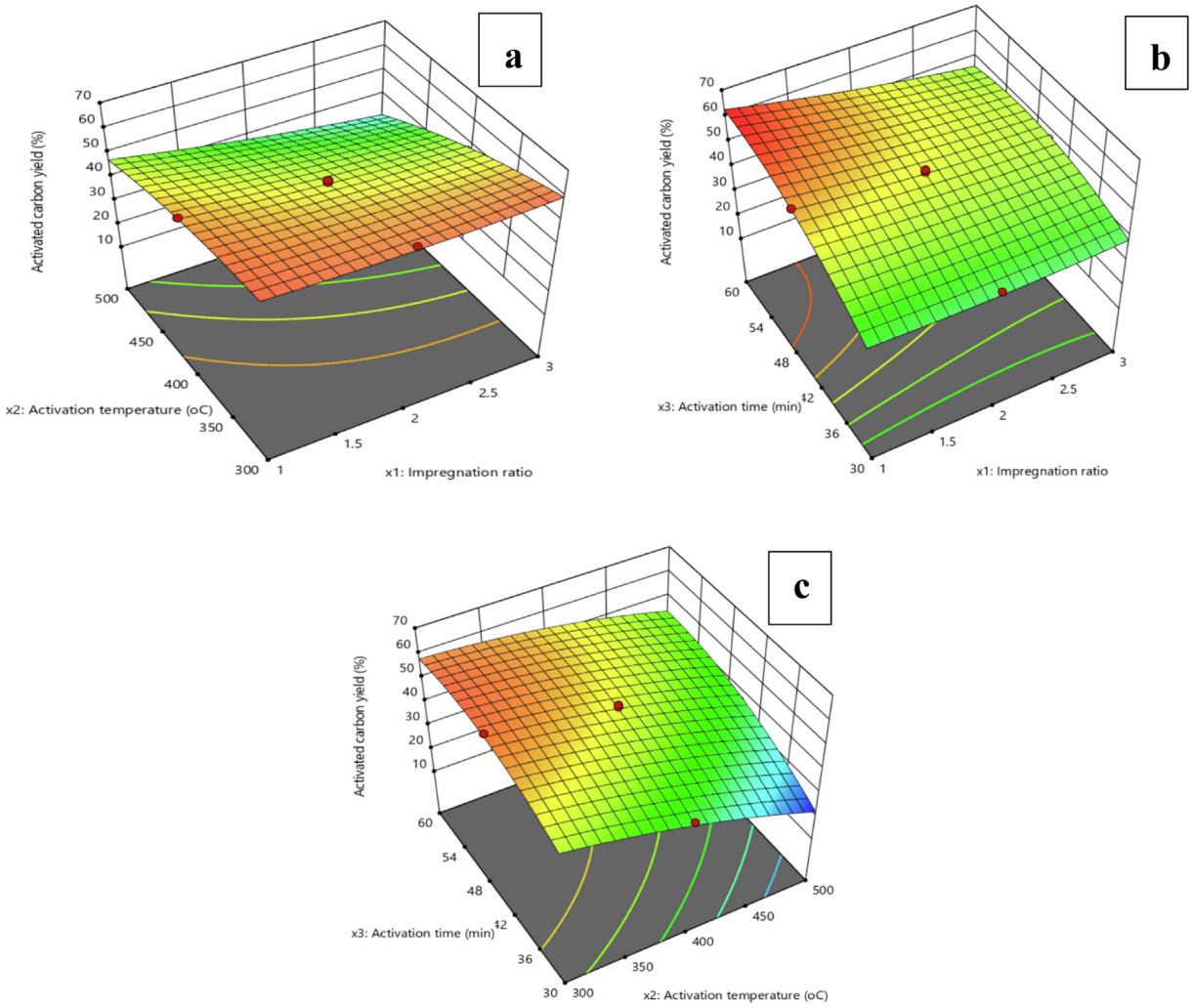

Fig. 1. Response surface plots for (a) impregnation ratio and activation temperature (b) activation time and impregnation ratio (c) activation time and activation temperature on HBAC percentage yield.

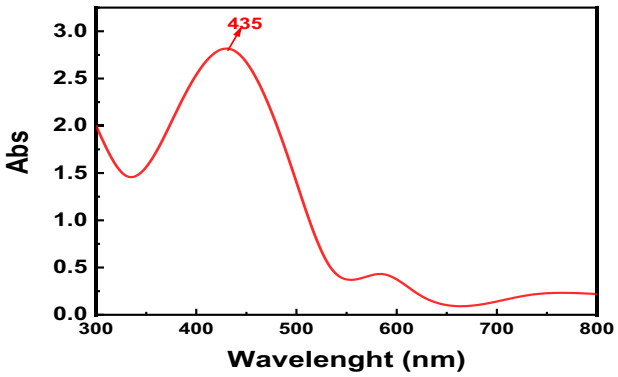

Fig. 2. UV–vis absorbance spectra of biosynthesized AgNPs assisted by *O. gratissimum* leaf.

verified to achieve an overall yield of 59.412 with a desirability of 1.00.

3.2. Characterizations of AgNPS, HBAC and AgNPs/HBAC

3.2.1. UV–Vis spectroscopy

The UV–Vis spectra of AgNPs is shown in Fig. 2, which clearly demonstrated a Surface Plasmon resonance of silver at absorption band of 435 nm. This finding was consistent with the findings of Al-Otibi et al., [57], who used *Malva parviflora* to biosynthesize AgNPs.

The secondary metabolites of *O. gratissimum* extract revealed the presence of bioactive compounds such as phenol, alkaloids, steroids, saponins, glycosides, and flavonoids as presented in **Table S5**. The presence of these identified dominant phytochemical compounds in *O. gratissimum* extract may be assumed to be the primary reducing and stabilizing agents in the biosynthesis of AgNPs [58].

3.2.2. SEM analysis

The SEM micrographs of the developed samples at different magnifications were depicted in Fig. 3. The SEM images presented in Fig. 3**(a-c)**, showed the formation of a clear homogeneous, smooth and well- arranged large pores in forms of pores and caves forming a honey-comb structure [35]. The pores observed may be attributed to the KOH evaporation during carbonization [54]. Due to the porous nature of HBAC, additional loading space for AgNPs may be possible [59]. The EDX spectrum of HBAC as shown in Fig. 3**(d)**, confirms the chemical composition of prepared HBAC with the carbon (66.36 %) and oxygen (24.73 %) content found in significant amount while the percentage weight of other elements was seen in a traceable amount, confirming the development of

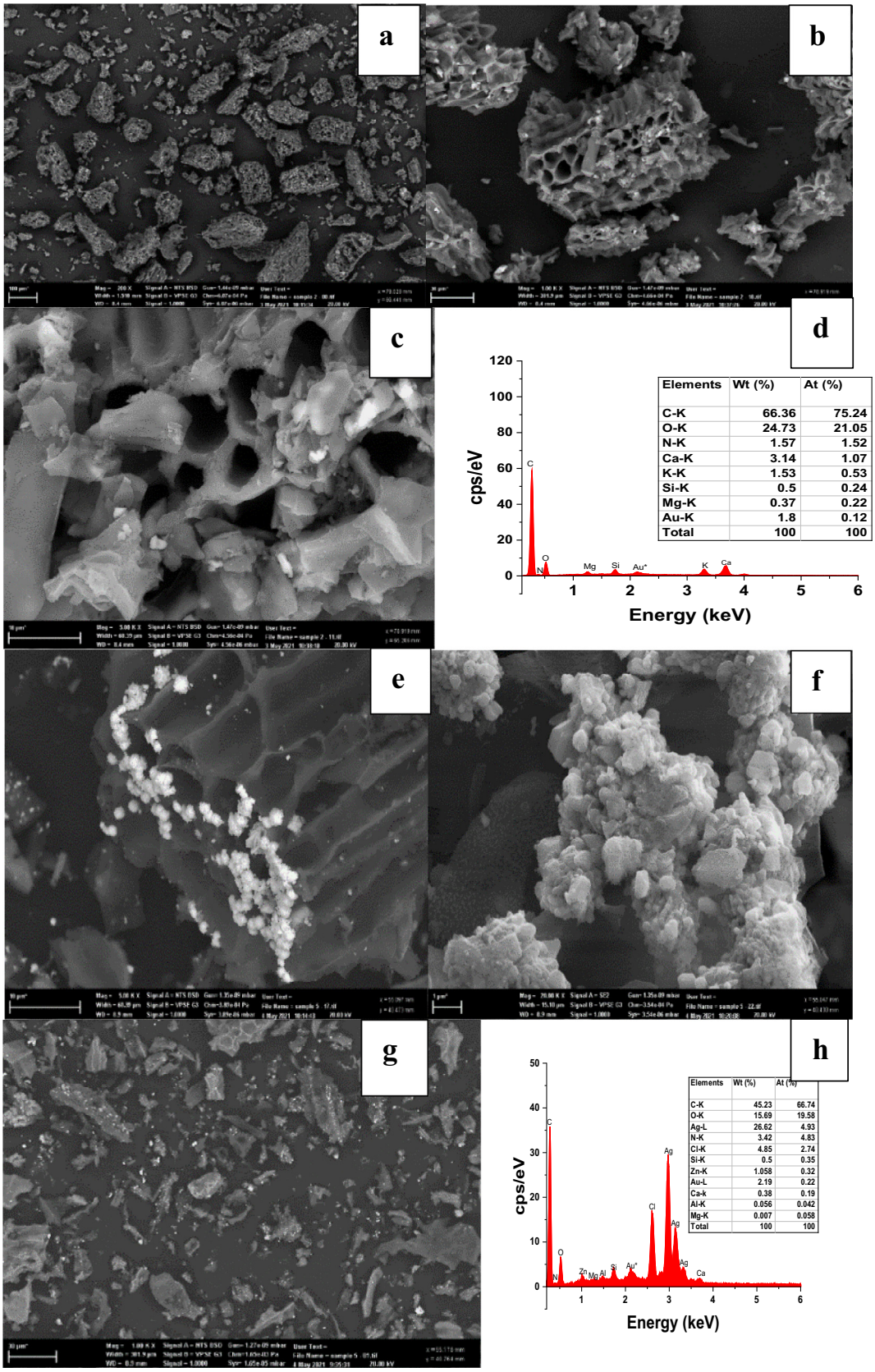

Elements	Wt (%)	At (%)
C-K	66.36	75.24
O-K	24.73	21.05
N-K	1.57	1.52
Ca-K	3.14	1.07
K-K	1.53	0.53
Si-K	0.5	0.24
Mg-K	0.37	0.22
Au-K	1.8	0.12
Total	100	100

Elements	Wt (%)	At (%)
C-K	45.23	66.74
O-K	15.69	19.58
Ag-L	26.62	4.93
N-K	3.42	4.83
Cl-K	4.85	2.74
Si-K	0.5	0.35
Zn-K	1.058	0.32
Au-L	2.19	0.22
Ca-k	0.38	0.19
Al-K	0.056	0.042
Mg-K	0.007	0.058
Total	100	100

Fig. 3. SEM micrographs at different magnifications and EDX analysis for (a-d) HBAC, and (e-h) AgNPs/HBAC.

HBAC. The SEM micrographs of AgNPs/HBAC were presented in Fig. 3**(e-g)**. The presence of AgNPs in the form of white spots was seen on the surface and pores of the HBAC external surface [60]. Despite the fact that some of the HBAC pores have been occupied

by AgNPs, HBAC still has a large pore volume and a porous structure that can easily facilitate adsorbates transfer into the inner surface of the adsorbents [61]. The identification of elements present in the AgNPs/HBAC was revealed by the EDX analysis. When the EDX analysis of AgNPs/HBAC (Fig. 3**(h)**) is compared to that of HBAC (Fig. 3**(d)**), it was clear that AgNPs were successfully loaded on the surface of HBAC, as evidenced by the decrease in carbon and oxygen content of HBAC. HBAC/AgNPs had an elemental composition of 45.23 % carbon, 15.69 % oxygen, and 26.62 % Ag.

3.2.3. TEM analysis

TEM images at different magnification for HBAC, AgNPs, and AgNPs/HBAC were depicted in Fig. 4. The TEM images as depicted in Fig. 4**(a-d)** confirmed that the HBAC developed has a highly porous structure with well-confined pores, confirming the amorphous nature of the material [62]. The TEM images of AgNPs obtained, as shown in Fig. 4**(e-g)**, revealed that the particles are polydispersed without agglomeration and are primarily spherical in shape [63]. The bioactive compounds trapped on the surface of AgNPs can be attributed to the AgNPs surrounding thin layer [64]. The particle sizes of AgNPs ranged from 6 to 24 nm, with an average particle size of 15.57 nm. The TEM micrograph of HBAC/AgNPs is given in Fig. 4**(i-l)**. The images demonstrated that AgNPs were successfully loaded onto the HBAC matrix. The images of the AgNPs/HBAC nanocomposite had a spherical shape, indicating the formation of AgNPs on the HBAC [35]. AgNPs/HBAC have an average particle size of 26.36 nm and a particle size range of 22–43 nm.

3.2.4. XRD analysis

The crystallinity of HBAC, AgNPs and AgNPs/HBAC was examined using the XRD pattern, as presented in Fig. 5. The developed HBAC at optimum conditions exhibits three broad diffraction peaks at $2\theta = 24.09°$, 42.79°, and 57.18°, which correspond to (002), (100), and (004) diffraction as presented in Fig. 5**(a)**. Graphitization of carbon materials appears to be the result of the peak at (002) during the development of activated carbon, confirming the amorphous nature of the synthesized HBAC material [35,6]. The XRD pattern of AgNPs as depicted in Fig. 5**(b)**, displays four intense diffraction peaks at 2θ, 38.11°, 44.25°, 64.43°, and 77.35° conforming to the (111), (200), (220), and (311) planes, which is consistent with silver nanocrystals standard patterns (JCPDS file No. 0.4–0.783) with face-centered cubic crystal structure [65,31]. The synthesized AgNPs size was evaluated using the Debye-Scherrer equation.

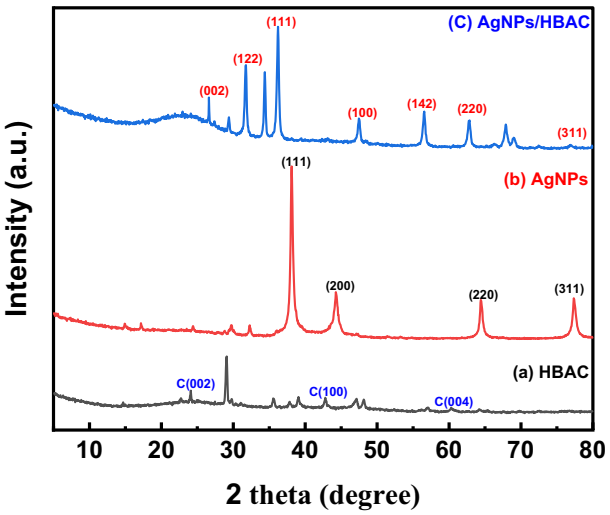

Fig. 5. XRD analysis patterns for (a) HBAC, (b) AgNPs, and (c) AgNPs/HBAC.

$$D = \frac{0.9\lambda}{\beta \cos\theta} \tag{9}$$

where D is the AgNPs crystalline size, λ is the wavelength (0.1541 nm), β is the average full width half maximum (FWHM) and θ is the diffraction angle. The average crystalline size of the synthesized AgNPs was calculated to be 23.11 nm. [65]. The AgNPs/HBAC XRD pattern, depicted in Fig. 5**(c)**, also shows strong diffraction peaks at 2θ, 26.61°, 31.75°, 36.22°, 47.51°, 56.65°, 62.85°, and 77.01°, corresponding to (002), (122), (111), (100), (142), (220), and (311) crystal planes of AgNPs and HBAC. This result demonstrated that AgNPs were successfully immobilized on the surface of HBAC [66].

3.2.5. FTIR analysis

The FT-IR-spectrum of AgNPs, HBAC, and AgNPs/HBAC are depicted in Fig. 6. The FT-IR spectra of biosynthesized AgNPS from *O. gratissimum* leaf extract given in Fig. 6**(a)**, shows an absorption peak at 3389 cm^{-1} that is related to N-H stretching. C–H stretching of alkane groups is responsible for the peak at 2935 cm^{-1}. The more intense absorption band seen at 1643 and 1427 cm^{-1} can be attributed to amide C=O stretching vibrations caused by carbonyl stretch in protein. The C-H bending is described by the peak

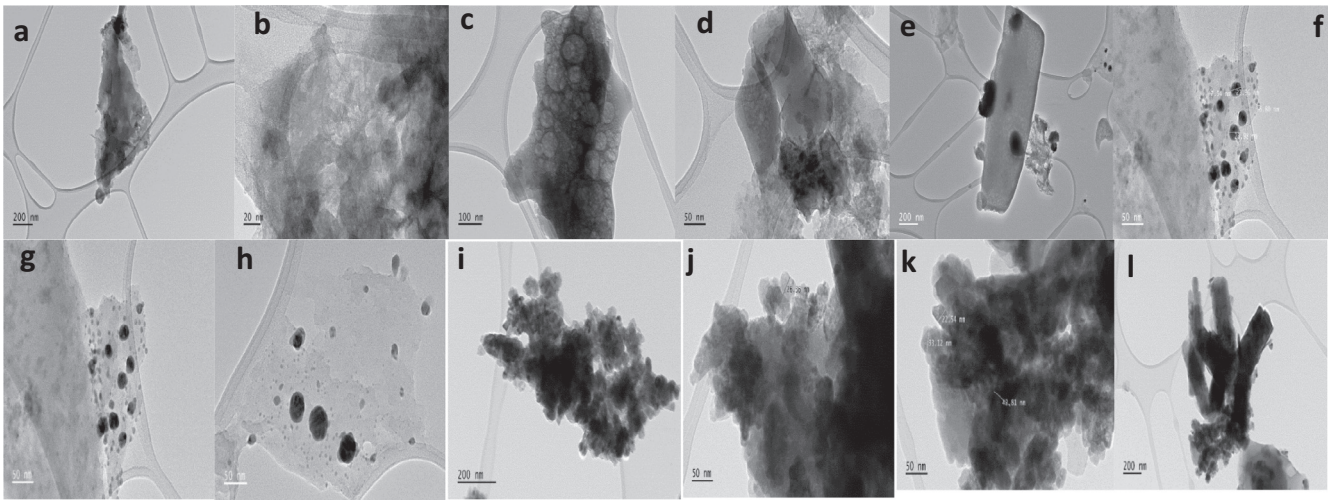

Fig. 4. TEM images for (a-d) HBAC, (e-h) biosynthesized AgNPS from *O. gratissimum* leaf extract, (i-l) AgNPs/HBAC.

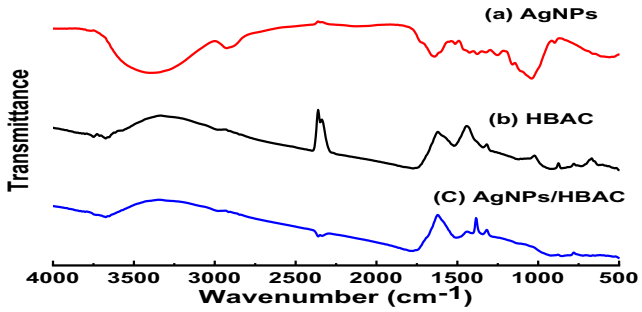

Fig. 6. FT-IR analysis for (a) AgNPs, (b) HBAC, and (c) AgNPs/HBAC.

at 1377 cm^{-1}. The aliphatic amine C-N stretching is responsible for the peak at 1257 cm^{-1}. C–O bonds are ascribed to the absorption bands at 1041 and 896 cm^{-1} [67]. The presence of organic compounds on the surface of the biosynthesized AgNPs from *O. gratissimum* leaf extract was confirmed by these FT-IR results. Functional groups like C-N, N-H, and C=O may be responsible for the bioreduction of Ag+ to AgNPs [68]. HBAC FT-IR spectra depicted in Fig. 6**(b)** shows some absorption peaks at 3749, 3675, and 3568 cm^{-1} relating to –OH stretching vibration of alcohols, phenols, and adsorbed water. The band at 2989 cm^{-1} is assigned to C–H stretching of alkenes and alkanes, implying that the HBAC has been completely carbonized [69]. CH_2 stretching is responsible for the band at 2387 cm^{-1}. The C=O carbonyl groups are represented by a broad absorption peak at 1736 cm^{-1}. The peak at 1520 cm^{-1} can be attributed to a C=C stretching aromatic ring. The C–O stretching vibrations in esters, ethers, phenols, alcohols, and acids are responsible for the intense absorption peak at 1141 cm^{-1}. The bands at 737 and 633 cm^{-1} aided in the out-of-plane bending of C-H in benzene derivatives. FTIR spectra of AgNps-HBAC as presented Fig. 6**(c)** shows similar absorption peaks with HBAC at 3748, 3675, 2989, 1736 and 1520 cm^{-1}. The absorption peaks at 2360, 1404, 1343, 1292, 926 and 856 cm^{-1} are apparent when AgNPS was loaded on HBAC surface.

3.2.6. BET analysis

The BET analysis plots for HBAC and AgNPs/HBAC were presented in Fig. 7. The BET surface areas of HBAC and AgNPs/HBAC were 822 and 794 m^2/g, respectively, with total pore volumes of 0.616 and 0.462 cm^3/g and average pore sizes of 6.194 and 5.154 nm. The HBAC high BET surface area was attributed to potassium metal intercalation via the intermediate reaction of KOH with carbon. The lower BET surface area value of AgNPs/HBAC could be attributed to AgNPs addition on the HBAC surface, which causes pore blockage of the AgNPs/HBAC [59,70]. The result revealed that the AgNPs successfully percolated and incorporated into the HBAC matrix, resulting in the formation of AgNPs/HBAC. AgNPs/HBAC would be advantageous in that they would be bi-functional in nature, targeting both large molecule pollutants and acting as an antimicrobial agent. According to IUPAC classifications, the HBAC and AgNPs/HBAC exhibited behavior of both Type II and IV isotherms as depicted in Fig. 7**(a &c)**, indicating that the HBAC and AgNPs/HBAC composite is nonporous and mesoporous in nature. The pore size distributions for HBAC and AgNPs/HBAC as calculated by BJH were seen in Fig. 7**(b &d)**. The pore size distribution of HBAC and AgNPs/HBAC were discovered to be in the range of 2–50 nm, indicating that the synthesized HBAC and AgNPs/HBAC nanocomposite is dominated majorly by mesopores [71].

3.2.7. pHzpc measurement

The pHpzc is defined as the pH of a solution at which the charge of the positive surface sites equals the charge of the negative ones, i.e., the adsorbent surface charge has no value [72]. The surface charge is negative when the pH is greater than pHpzc and positive when the pH is less than pHpzc. The solid addition method, as described by Auta and Hameed, [54] was used to determine the point zero surface charge of the AgNPs/HBAC characteristics. 50 mL of 0.1 M NaCl was measured into six 100 mL conical flasks with glass stoppers before adding 0.1 g AgNPS/HBAC.

The pH of the prepared NaCl solutions was adjusted between 2 and 12 using 0.1 M NaOH or 0.1 M HCl. The samples were placed on a mechanical shaker at 140 rpm for 24 h. At the expiration of time, when equilibrium was established between the NaCl solution and the AgNPs/HBAC, the final pH readings were noted. The pH_i-pH_f values were plotted against the initial pH values of the solution, and the corresponding pH reading was taken as the pHzpc of AgNPs/HBAC at the point where the plot crosses the point zero line. Therefore, the pHzpc of AgNPs/HBAC as shown in **Fig. S2** was 7.8 implying that AgNPs/HBAC surface is positively charged at pH values below the pHzpc and negatively charged above this point.

3.3. AgNPs/HBAC antibacterial activity

The AgNPs/HBAC was tested for antibacterial activity against *Pseudomonas aeruginosa, Salmonella typhi, and Escherichia coli* (Gram negative) and against *Bacillus subtilis* (Gram positive) at 25, 50 and 100 mg/mL using Agar-well diffusion (Muller Hinton Agar) method described by Qu et al., [73]. Each well had a diameter of 9 mm, with DMSO serving as negative control and streptomycin (10 mg/mL) serving as positive control. The Petri dishes were allowed to stand for a while after transferring 100 mL of each concentration into the wells before incubating for 24 h at 37 °C. The diameters of the zones of inhibition were measured in each plate, and the mean values were recorded. According to the mean values presented in **Table S6**, it was observed that *Pseudomonas* was the most susceptible to HBAC-AgNPs when compared to *B. subtilis, E. coli, and Salmonella sp*. However, at 100 mg/mL, *B. subtilis* showed greater susceptibility to the AgNPs/HBAC than at 25 and 50 mg/mL.

3.4. Influence of adsorption parameters on CR removal

The solution pH is an important parameter in adsorption processes especially in determining the percentage removal. The effect of the initial pH of solution on CR dye removal by AgNPs/HBAC is shown in Fig. 8**(a)**. An investigation of the effect of pH on adsorption of CR was carried out at pH range of 2–10 for 4 h. The climax of adsorption was attained at lowest pH 2 and the least removal was obtained at pH 10. This can be attributed to the fact that at lower pH, CR dye exist as an anionic molecule and contains a negatively charged group (–$SO3^-$ Na^+). In acidic media CR dissociates into (R–$SO3^-$) which promotes its sorption to the positive surface of the sorbent (AgNPs/HBAC) via strong electrostatic force [74]. Furthermore, in acidic conditions, sorbent binding sites are closely associated with hydrogen ions, which act as bridging ligands between the adsorbent surface and the CR dye molecule for sorption [75]. In addition, due to surface complexation between the CR dye molecules and the O-H functional group, high removal was observed in acidic medium. At higher pH, however, there is an increase in negative ions (OH), which compete for sorption sites with CR dye molecules, resulting in a decrease in the removal efficiency. As a result of the reduced positive charge on the sorbents and the weakened electrostatic attraction between the sorbent surfaces and the CR dye molecule, the removal efficiency decreases [76].

Another important parameter in batch process adsorption that can influence the adsorption behavior CR dye onto AgNPs/HBAC is contact time. The relationships of adsorption capacity and percentage on contact time for the removal of CR onto AgNPs/HBAC

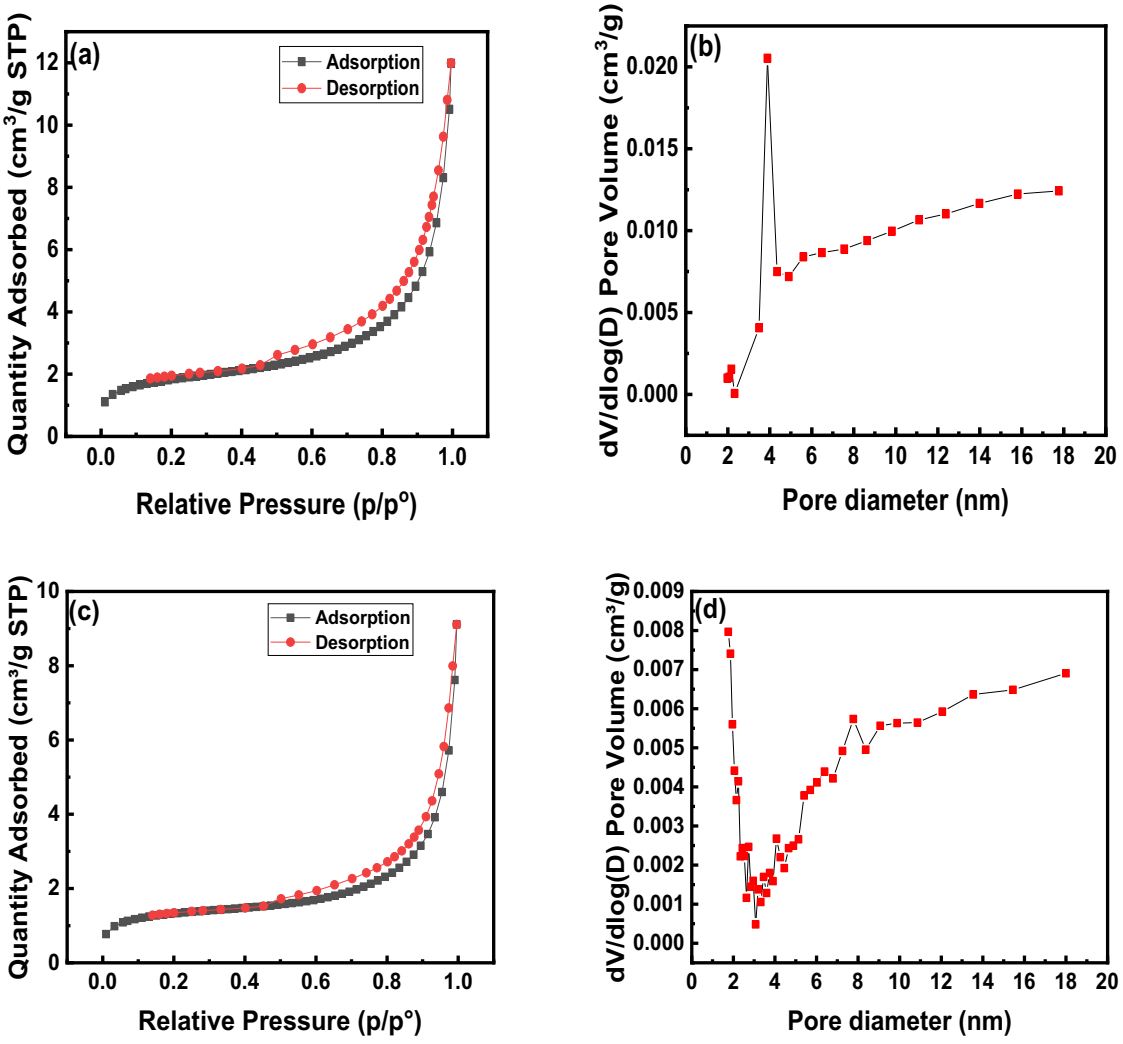

Fig. 7. BET analysis plots for (a-b) HBAC, (c-d) AgNPs/HBAC.

were investigated by varying the contact time up to 90 min, at pH 2.0, with varying initial CR concentration (20–100 mg/L), at 308 K, and 100 mg adsorbent dosage. According to the plots in Fig. 8(**b &c**), increasing CR concentration resulted in significant adsorption capacity increase in the initial stage and attained a dynamic equilibrium, whereas increasing CR concentration resulted in a decrease in percentage removal [77]. This finding can be attributed fact that the higher the initial concentration of CR, the greater the driving force for mass transfer, resulting in an increase in the adsorption capacity of CR [78]. The adsorption capacity increased significantly from 18.86 to 89.64 mg/g at equilibrium as the CR concentration increased from 20 to 100 mg/g (Fig. 8(**b**)). However, the decrease in CR percentage removal as concentration increases could be attributed to adsorbent site saturation on the adsorbent's surface [79]. Excess pollutant concentration may result in a decrease in CR percentage removal due to AgNPs/HBAC active surface limitation and saturation [80]. As observed in Fig. 8(**c**), as the CR concentration increases from 20 to 100 mg/L, the percentage removal of CR decreases from 99.42 to 89.64 % [47]. As a result, the removal of CR onto AgNPs/HBAC composite increased with time and reached equilibrium at 60 min, which was used for further investigation.

Adsorbent dosage effect on CR removal onto AgNPs/HBAC was investigated in order to determine adsorbent effectiveness and the ability to adsorb CR with a minimum dosage. This study was carried out with an initial CR concentration of 100 mg/L, a pH of 2.0, an equilibrium time of 60 min at 308 K, and varying adsorbent dosage (0.1–1 g), as shown in Fig. 8(**d**). The percentage removal of CR increased from 78.88 to 98.87 % as the AgNPs/HBAC dosage was increased from 0.1 to 0.4 g. This is as result of the increased availability of active sites on the AgNPs/HBAC surface that can interact with the CR as the dosage increases. However, increasing the AgNPs/HBAC concentration (>0.4 g) resulted in no significant increase in CR removal due to AgNPs/HBAC saturation by the CR molecules. This observation can also be attributed to the fact that the amount of possible active sites on the adsorbent surface increased with increasing adsorbent dosage and, to some extent, attain equilibrium due to agglomeration of the adsorbent surface sites with increasing adsorbent dosage [81].

The temperature CR removal onto AgNPs/HBAC was investigated by varying the temperature from 298 to 323 K, with 100 mg/L initial CR concentration, a pH of 2.0-, and 60 min equilibrium time, as shown in Fig. 8(**e**). The results showed that as the temperature increased from 303 to 323 K, the CR removal decreased from 98.67 to 51.67 %. This could be attributed to AgNPs/HBAC active site damage caused by an increase in kinetic energy of the molecules as temperature rises, resulting in a decrease in electrostatic interaction between the CR and AgNPs/HBAC [78]. This finding revealed that the adsorption of CR onto AgNPs/HBAC is exothermic [82].

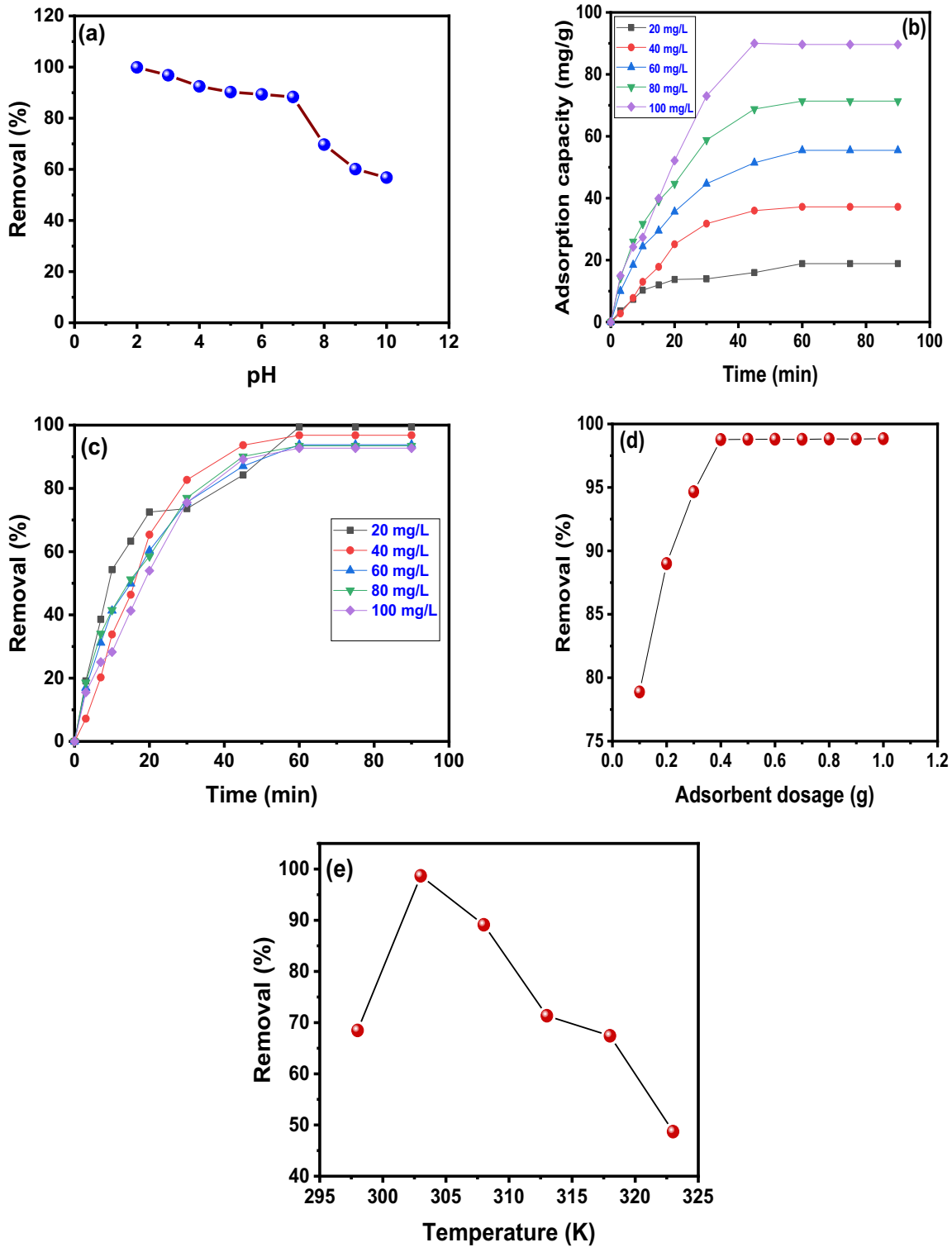

Fig. 8. Effect of adsorption parameters (a) pH, (b & c) contact time, (d) adsorbent dosage, and (e) temperature on CR removal.

3.5. Adsorption isotherm

The interaction mechanism between the adsorbate and adsorbent was investigated using the adsorption isotherms described by Langmuir, Freundlich, Temkin, and Dubinin–Radushkevich (D-R). The adsorption isotherm models also provide information on the adsorbate distribution between the adsorbent surface when the adsorption process has attained equilibrium. Table 1 shows the equations for the adsorption isotherm models studied. The Langmuir model is based on the assumption of monolayer adsorption on a homogeneous surface with identical active sites [83]. The Freundlich model is based on the assumption of surface heterogeneity between the adsorbent and adsorbate [84]. The Temkin model assumes that adsorption is characterized by a uniform distribution of binding energies and that increased coverage due to adsorbate-adsorbent interaction results in a decrease in heat of

Table 1
Adsorption Isotherm models.

Models	Equation	Plot	Parameters	References
Langmuir	$\frac{C_e}{q_e}=\frac{1}{q_m K_L}+\frac{C_e}{q_m}$	$\frac{C_e}{q_e}$ vsC_e	q_m, K_L	Langmuir, [83]
Freundlich	$logq_e = logK_F + \frac{1}{n} logC_e$	$logq_e$ $vslogC_e$	$K_F, \frac{1}{n}$	Freundlich, [84]
Temkin	$q_e = BlnK_T + BlnC_e$	q_e $vslnC_e$	A_T, B	Tempkin and Pyzhev, [85]
Dubinin-Radushkevich (D-R)	$\ln(q_e) = \ln(q_s) - \beta\varepsilon^2$ $E = \frac{1}{\sqrt{2\beta}}$	lnq_e $vs\varepsilon^2$	q_s, β, E	Dubinin and Radushkevich, [86]

adsorption [85]. Dubinin–Radushkevich model was employed to estimate the porosity characteristic and free energy of adsorption. It also aids in determining the physical or chemical nature of adsorption processes [86]. The D-R model's adsorption mean free energy (E) assumes physical adsorption when the value of E < 8 kJ/-mol and chemical adsorption when the value of E is 8 < E < 16 kJ/mol.

The amount of CR adsorbed per unit mass of AgNPs/HBAC was calculated using adsorption isotherm models as a function of the solute's equilibrium concentration in the bulk solution at constant temperature. Fig. 9 **(a, b, c & d)** depicts the linearized plots for Langmuir, Freundlich, Temkin, and Dubinin-Radushkevich.

When the regression correlation coefficient (R^2) and chi-square (χ^2) of each model were compared, it was observed that the Freundlich isotherm model best fit the CR dye adsorption onto AgNPs/HBAC better than the Langmuir, Temkin, and D-R models, with a higher R^2 and a smaller χ^2 values as shown in Table 2. The fitness of the Freundlich model to the adsorption of CR onto AgNPs/HBAC suggests a multilayer and heterogeneous adsorption process with different adsorbate affinity at each adsorption site [87]. The value of 1/n is a measure of surface heterogeneity, with values ranging from 0 to 1 becoming more heterogeneous as the value approaches zero. [9]. According to the calculated 1/n value of 0.7032, the adsorption surface of AgNPs/HBAC was heterogeneous in nature and favoured CR dye adsorption [61]. The monolayer adsorption capacity calculated from Langmuir adsorption isotherm model was 161.290 mg/g. The D-R isotherm demonstrated that the adsorption process is physical, as evidenced by a mean free energy (E) of less than 8 kJ/mol. The maximum adsorption capacities of CR onto different adsorbents reported in literature is shown in Table 3.

3.6. Adsorption kinetics

The kinetics of CR dye adsorption onto AgNPs/HBAC at different CR initial concentrations were investigated by fitting the adsorp-

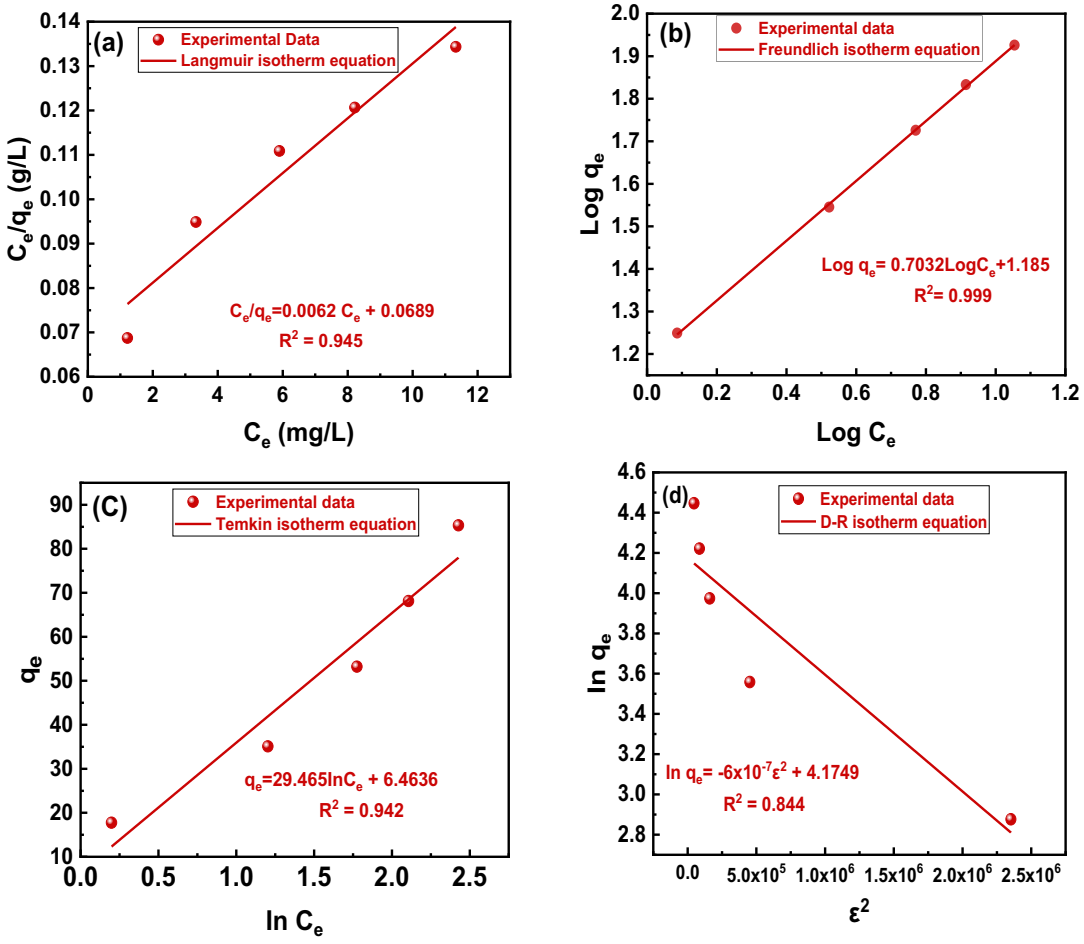

Fig. 9. Adsorption isotherm model plots for (a) Langmuir, (b) Freundlich, (c) Temkin and (d) D-R.

Table 2
Isotherms parameters for CR dye adsorption on AgNPS/HBAC.

Isotherm	$q_m (mg/g)$	K_L **(L/mg)**	R^2	χ^2	
Langmuir	161.290	0.0900	0.945	0.316	
	K_F	**1/*n***	R^2	χ^2	
Freundlich	74.557	0.732	0.999	0.141	
	k_T **(L/mg)**	***B***	R^2	χ^2	
Temkin	1.245	29.465	0.942	2.430	
	$q_s (mg/g)$	$\beta\left(mol^2/J^2\right) \times 10^{-7}$	**E(kJ/mol)**	R^2	χ^2
Dubinin–Radushkevich	65.0333	6.000	0.913	0.844	3.161

Table 3
Comparison of CR maximum adsorption capacity onto various adsorbent.

S/n	Adsorbent	Maximum adsorption capacity (mg/g)	References
1.	Biosynthesized ZnONPs from *Hibiscus rosa-sinensis* extract	9.62	[97]
2.	Litchi seeds powder	20.49	[76]
3.	Mesoporous activated carbon	14.20	[61]
4.	nanostructured spinel-type $ZnCr_2O_4$	62.53	[98]
5.	Ag-nBC	2.65	[99]
6.	*Antigonon leptopus* leaf powder	18.18	[106]
7.	Bentonite-ionic liquid composite (Bent_C_{12}mmCl)	150.0	[100]
8	nZVMn/PBC	117.65	[101]
9	Curcumin conjugated zinc oxide nanoparticles (Zn(Cur)O)	89.85	[102]
10	AgNPs/HBAC	161.29	This study

tion data to four different models: pseudo-first order, pseudo-second order, Webber-Morris intraparticle and liquid film diffusion. The pseudo-first order assumes that physisorption controls the adsorption rate, whereas the pseudo-second order assumes that chemisorption controls the adsorption rate by transferring electron between the adsorbent and adsorbate [70]. The Webber-Morris Intraparticle diffusion method is commonly used to assess the adsorption rate after the initial stages of adsorption. Furthermore, liquid film diffusion assumes that the adsorbate molecule flows through a liquid film surrounding the adsorbent, which is the most time-consuming step in the adsorption process. [88]. The adsorption kinetic model equations investigated were presented in Table 4.

Where k_1 is the pseudo-first-rate constant (min^{-1}), k_2 is the pseudo-second order rate constant (g/mgmin), kp is the Webber-Morris intraparticle diffusion rate constant (mg/g $min^{1/2}$), K_F (min^{-1}) is the liquid film diffusion rate constant, C is the rate constant diffusion, and F is the equilibrium fractional attainment. The pseudo -first and second order, Webber-Morris intraparticle, and liquid film diffusion kinetic model curves drawn from experimental data are shown in Fig. 10 **(a, b, c, & d)**. The summary of the results evaluated from the slopes and intercepts of the corresponding regression curves, with the parameters k_1, k_2, q_e, k_p, K_F, C, and R^2 is presented in Tables 5 and 6. When the pseudo-first and second order kinetics were compared, it was clear that the pseudo-second order kinetic had a higher R^2 values than the pseudo-first order kinetic. The pseudo-second order model also revealed that the adsorption capacity values calculated q_e (cal) from the slopes and intercepts are closer to the experimental values qe (exp). The decrease in the adsorption rate constant (k_2) of the pseudo-second order model as the initial CR concentration increased suggests that CR dye adsorption onto AgNPs/HBAC reached equilibrium faster at lower concentrations than at higher concentrations [89,90]. This finding showed that chemisorption dominates and controls CR adsorption onto AgNPs/HBAC, and that the interaction between the CR and AgNPs/HBAC involves electron exchange or sharing [91]. Qin et al., [92] made a similar observation when they synthesized a novel CaCO3/chitin aerogel for CR removal.

The multi-linearity curve of the Webber-Morris intraparticle diffusion model depicted in Fig. 10**(c)**, showed that the adsorption of CR onto AgNPs/HBAC is controlled by two or more adsorption mechanism steps. In the first phase, CR molecules diffuse into the AgNPs/HBAC outer surface; in the second phase, CR molecules diffuse into the AgNPs/HBAC internal pores (liquid film diffusion); and in the third phase, CR molecules deplete due to the adsorption mechanism, which is regulated by intra-particle diffusion (adsorption equilibrium stage). Using the Webber-Morris intraparticle fitting curve, it was found that intraparticle diffusion (pore diffusion) is not the only rate-controlling step during adsorption, but that other processes, such as liquid film diffusion, may also be involved in the adsorption process [93]. The Webber-Morris constant, C, was shown (see Table 6) increased as the initial CR concentration increases. This is due to the fact that AgNPs/HBAC boundary layer has grown in thickness [94].

The evaluated kinetics data revealed the pseudo-second order fitness in describing the procedure of CR adsorption onto AgNPs/HBAC. Although the adsorbent adsorption surface, liquid film diffusion, and intraparticle diffusion, are all included in the overall adsorption process. Due to the rapid adsorption process, the adsorption response cannot be regarded a controlling step. As a

Table 4
Adsorption Kinetic models.

Kinetic models	Linear form	Plot	Parameters	Reference
Pseudo-first-order	$log(q_e - q_t) = log q_e - \frac{k_1 t}{2.303}$	$log(q_e - q_t)$ vs t	$q_{e,cal}, k_1$	[96]
Pseudo-second- order	$\frac{t}{q_t} = \frac{t}{q_e} + \frac{1}{k_2 q_e^2}$	$\frac{t}{q_t}$ vs t	$q_{e,cal}, k_2$	[103]
Webber-Morris intra-particle diffusion	$q_t = k_p t^{0.5} + C$	q_t vs $t^{0.5}$	k_p, C	[104]
Liquid film diffusion	$-ln(1-F) = K_F t + CF = \frac{q_t}{q_e}$	$\ln(1-F)$ *vst*	K_F, C	[105]

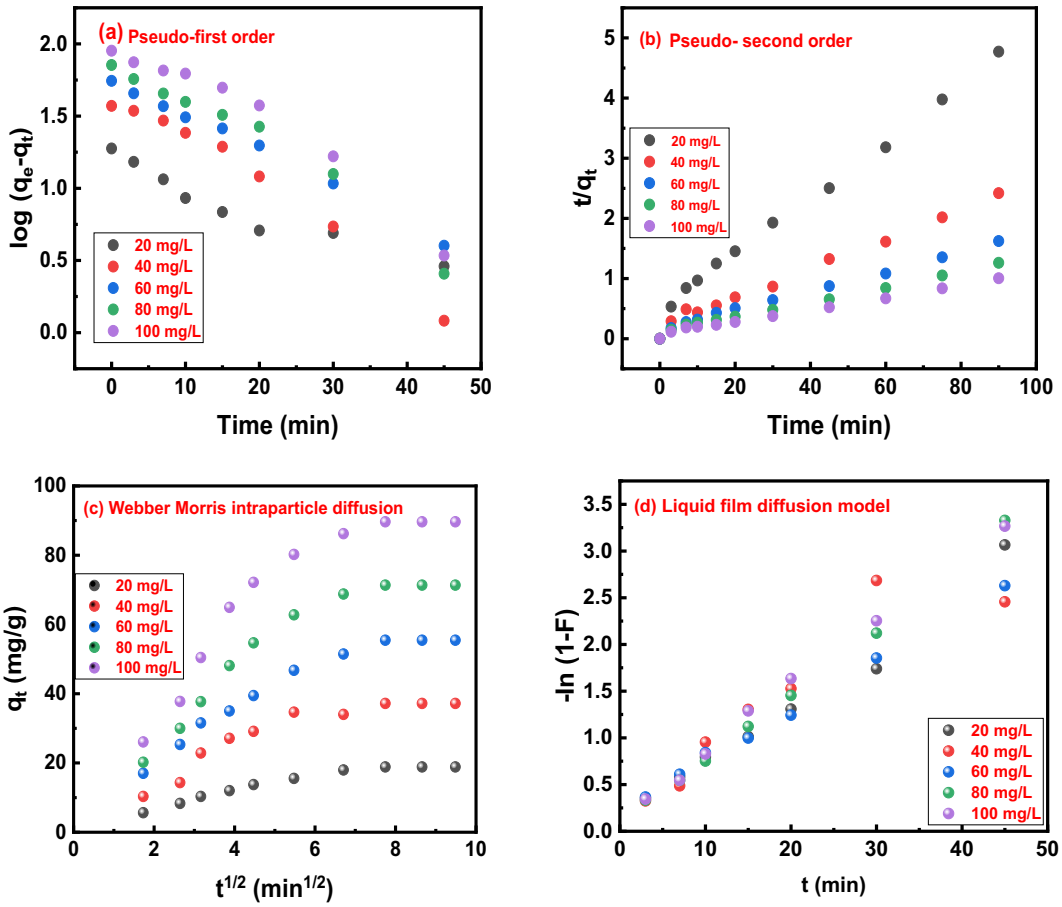

Fig. 10. Kinetic models fitting curves for (a) pseudo-first order, (b) pseudo-second order, (c) Webber-Morris intraparticle diffusion, and (d) liquid film diffusion.

Table 5
Pseudo-first and second order kinetics parameters for CR adsorption onto AgNPs/HBAC.

Dye Conc. (mg/L)		Pseudo-first order model			Pseudo-second order model		
	q_e (mg/g)	q_e (mg/g)	k_1 (min-1)	R^2	q_e (mg/g)	k_2 (g/mg min)	R^2
20	18.86	14.99	0.00401	0.915	20.66	0.00609	0.990
40	37.20	48.43	0.0767	0.976	40.48	0.00351	0.990
60	55.45	56.68	0.0571	0.995	60.61	0.00213	0.991
80	71.35	80.58	0.0698	0.964	78.13	0.00167	0.990
100	89.64	112.95	0.0702	0.951	97.087	0.00151	0.992

Table 6
Webber-Morris and liquid film diffusion models for CR adsorption onto AgNPs/HBAC.

Dye Conc. (mg/L)		Webber-Morris Intra-particle diffusion			Liquid film diffusion		
	q_e (mg/g)	k_p	C	R^2	K_F	C	R^2
20	18.86	1.728	4.689	0.912	0.0619	0.116	0.982
40	37.20	3.320	10.487	0.818	0.0574	0.326	0.856
60	55.45	4.971	14.470	0.918	0.0533	0.231	0.997
80	71.35	6.630	17.857	0.872	0.0713	0.0543	0.998
100	89.64	8.022	25.381	0.840	0.0704	0.145	0.996

result, gradual steps including intra-particle diffusion and liquid film diffusion, whether individually or collectively, controlled the adsorption process [92]. For mass transfer of CR adsorption onto AgNPs/HBAC as indicated in Fig. 10**(d),** the liquid film diffusion model was shown to be more appropriate based on the R^2 values obtained for intraparticle and liquid film diffusion. Finally, the rate of CR dye adsorption onto AgNPs/HBAC is controlled by liquid film and intraparticle diffusion, thereby allowing the adsorption to fit the Pseudo-second order kinetic model [95].

3.7. Adsorption thermodynamics

The adsorption thermodynamics parameters such as enthalpy change (ΔH), Gibbs free energy (ΔG), and entropy change (ΔS) were

Table 7
Thermodynamic parameters of CR adsorption onto AgNPs/HBAC.

Dye conc. (mg/L)	ΔH(kJ/mol)	ΔS(J/mol K)	E_a (kJ/mol)	ΔG (kJ/mol)		
				308 K	**318 K**	**328 K**
20	−58.088	−166.712	28.493	−6.741	−5.074	−3.407
40	−35.143	−94.405	14.347	−6.067	−5.122	−4.178
60	−21.722	−52.418	10.896	−5.578	−5.054	−4.530
80	−24.043	−60.382	17.598	−5.446	−4.842	−4.238
100	−23.665	−60.173	11.867	−5.133	−4.531	−3.929

evaluated to determine the feasibility and spontaneity of the adsorption process. Using the relationship between the equations, the Gibbs free energy (G) was determined;

$$\Delta G = -RT \ln K_0 \tag{10}$$

$$\Delta G = \Delta H - T\Delta S \tag{11}$$

$$K_0 = \frac{q_e}{C_e} \tag{12}$$

where K_0 is related to thermodynamic equilibrium constant, T is the absolute temperature (K) and R is the gas constant (8.314 J/mol K). The $\Delta S and \Delta H$ values are evaluated using the equation;

$$\ln K_0 = \frac{\Delta S}{R} - \frac{\Delta H}{RT} \tag{13}$$

The plot of $\ln K_0$ against 1/T at different concentrations yields a straight-line graph as depicted in **Fig. S3(a)**, and the $\Delta S and \Delta H$ values were evaluated at different CR concentration from the intercepts and slopes of the graph. Table 7 demonstrates the thermodynamic adsorption results for CR adsorption onto AgNPs/HBAC at various concentrations. The adsorption of CR onto AgNPs/HBAC was feasible, spontaneous, and thermodynamically favourable as result of the negative ΔG values obtained [76]. The negative values of ΔH and ΔS suggests exothermic and randomness decreased at the adsorbate-adsorbent interface during the adsorption of CR onto AgNPs/HBAC. According to the thermodynamic data, adsorption performance of AgNPs/HBAC towards CR molecules was favoured at low temperatures.

The activation energy of CR adsorption onto AgNPs/HBAC was calculated for various concentrations using the rate constant of pseudo-second order kinetic (k_2) values as specified by the Arrhenius relation equation:

$$\ln k_2 = \frac{E_a}{R}\left(\frac{1}{T}\right) + constant \tag{14}$$

where E_a is the activation energy in kJ/ mol. The E_a values at various concentrations was estimated from the slope of the Arrhenius plot of $\ln k_2$ versus $1/T$. The E_a values between 5 and 40 kJ/mol assume physisorption whereas larger E_a values between 40 and 800 kJ/mol indicates chemisorption [107]. The calculated E_a values obtained from the slope depicted in **Fig. S2(b)** at various concentrations as shown in Table 7 was between 10.896 and 28.493 kJ/mol. This assumes that CR adsorption onto AgNPs/HBAC surface was more dominated by the physisorption.

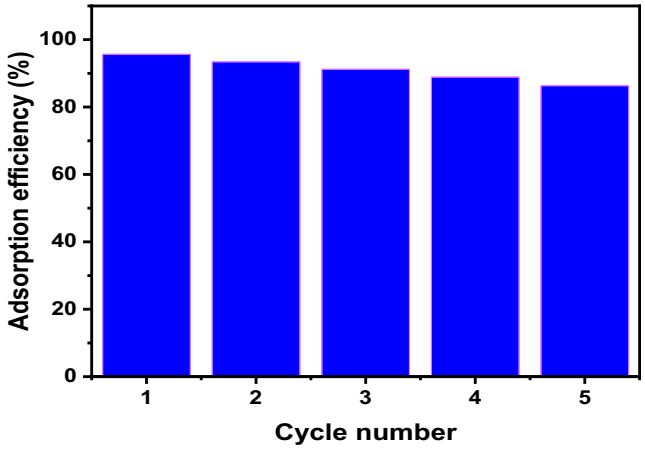

Fig. 11. Reusability of AgNPs/HBAC for the removal of CR.

3.8. AgNPs/HBAC regenerability and reusability study

The nature of regeneration and reusability of adsorbents generalizes their practical applicability. The goal of adsorbent regeneration is to make the adsorption process more environmentally friendly and cost effective. The results showed that after fifth consecutive cycle, the percentage removal of CR decreased from 95.66 to 86.34 %, as shown in Fig. 11. As a result of the experiment, it was observed that the AgNPs/HBAC has an excellent reuse potential with a reasonable economic value.

4. Conclusions

A central composite design which is an aspect of response surface methodology was utilized to optimize the development of high yield activated carbon from *Hildegardia barteri* (HBAC). The ANOVA result, which was used to determine the significance of independent variables and their interactions, revealed that impregnation ratio and time interaction had the greatest influence on the yield percentage. The optimum conditions determined by the design expert software were impregnation ratio of 1.078:1, activation temperature of 306.787, and activation time of 44.502, resulting in an overall percentage yield of 59.412 and a desirability of 1. Biosynthesized AgNPs from *Ocimum gratissimum* was successfully loaded on the optimized HBAC (AgNPs/HBAC) for the removal of congo red (CR) from aqueous solution. The textural, compositional, and structural properties of the developed AgNPs/HBAC were explained using XRD, SEM-EDX, FTIR, HRTEM, and BET. The adsor-

bent textural characterization revealed a BET surface area of 794 m^2/g, pore volume of 0.462 cm^3/g and pore diameter of 5.154 nm. The overall adsorption process was found to be influenced by adsorbent dosage, contact time, initial concentration, and temperature. The Langmuir, Freundlich, Temkin and Dubinin–Radushkevich isotherm models were investigated for the adsorption of CR onto AgNPs/HBAC, and the Freundlich model fitted well to the adsorption process. The maximum CR adsorption capacity onto AgNPs/HBAC was 161.290 mg/g. The kinetic models tested revealed that the adsorption process was best described by a pseudo-second order kinetic. The adsorption of CR was favoured by a decrease in temperature, implying that the adsorption process was exothermic. The regeneration and reusability of the AgNPs/HBAC composite was performed using ethanol and water as a desorbent, with an adsorption efficiency of removal percentage of 86.34 %t achieved after the fifth cycle. This demonstrated that AgNPs/HBAC can be regenerated efficiently and with high reusability. Antibacterial tests revealed that AgNPs/HBAC nanocomposites were effective against *Pseudomonas aeruginosa*, *Salmonella typhi, Escherichia coli*, and *Bacillus subtilis* bacteria.

CRediT authorship contribution statement

Kehinde Shola Obayomi: Conceptualization, Methodology, Software, Visualization, Writing – original draft, Validation, Data curation, Supervision, Funding acquisition. **Sie Yon Lau:** Funding acquisition, Writing – review & editing, Formal analysis, Supervision. **Divine Akubuo-Casmir:** Methodology, Data curation, Funding acquisition, Software. **Muibat Diekola Yahya:** Writing – review & editing, Supervision. **Manase Auta:** Supervision, Writing – review & editing. **A.S.M. Fazle Bari:** Funding acquisition, Formal analysis, Writing – review & editing. **Ayomide Elizabeth Oluwadiya:** . **Iyiola Oluwatobi Victoria:** Visualization, Software, Writing – review & editing. **Mohammad Mahmudur Rahman:** Funding acquisition, Writing – review & editing, Formal analysis, Supervision.

Declaration of Competing Interest

The authors declare that they have no known competing financial interests or personal relationships that could have appeared to influence the work reported in this paper.

Acknowledgements

The authors acknowledged Global Centre for Environmental Remediation (GCER), laboratory and EMX unit, The University of Newcastle, Callaghan, NSW 2308, Australia instrumental supports.

Appendix A. Supplementary material

Supplementary data to this article can be found online at https://doi.org/10.1016/j.molliq.2022.118735.

References

[1] S. Chen, R. Li, J. Qin, X. Guo, X. Chen, Fabrication of novel CuO/layered double oxide microspheres and its high efficiency adsorption performance for Congo red, Colloids Surf., A 622 (2021) 126649, https://doi.org/10.1016/j.colsurfa.2021.126649.
[2] Y. Achour, L. Bahsis, E.-H. Ablouh, H. Yazid, M.R. Laamari, M.E. Haddad, Insight into adsorption mechanism of Congo red dye onto Bombax Buonopozense bark activated-carbon using central composite design and DFT studies, Surf. Interfaces 23 (2021) 100977, https://doi.org/10.1016/j.surfin.2021.100977.
[3] A.K. Deb, B. Biswas, N. Goswami, E.F. Hilder, R. Naidu, M.M. Rahman, Synthesis of environmentally benign ultra-small copper nanoclusters-halloysite composites and their catalytic performance on contrasting azo dyes, Appl. Surf. Sci. 546 (2021) 149122, https://doi.org/10.1016/j.apsusc.2021.149122.
[4] A. Chowdhury, S. Kumari, A.A. Khan, S. Hussain, Synthesis of mixed phase crystalline CoNi2S4 nanomaterial and selective mechanism for adsorption of Congo red from aqueous solution, J. Environ. Chem. Eng. 9 (6) (2021) 106554.
[5] H. Wang, K. Yan, J. Chen, Preparation of hydroxyapatite microspheres by hydrothermal self-assembly of marine shell for effective adsorption of congo red, Mater. Lett. 304 (2021) 130573, https://doi.org/10.1016/j.matlet.2021.130573.
[6] K.S. Obayomi, A.E. Oluwadiya, S.Y. Lau, A.O. Dada, D. Akubuo-Casmir, T.A. Adelani-Akande, A.S.M. Fazle Bari, S.O. Temidayo, M.M. Rahman, Biosynthesis of Tithonia diversifolia leaf mediated Zinc Oxide Nanoparticles loaded with flamboyant pods (Delonix regia) for the treatment of Methylene Blue Wastewater, Arab. J. Chem. 14 (10) (2021) 103363, https://doi.org/10.1016/j.arabjc.2021.103363.
[7] M.E. González-López, C.M. Laureano-Anzaldo, A.A. Pérez-Fonseca, C. Gómez, J. R. Robledo-Ortíz, Congo red adsorption with cellulose-graphene nanoplatelets beads by differential column batch reactor, J. Environ. Chem. Eng. 9 (2) (2021) 105029, https://doi.org/10.1016/j.jece:2021.105029.
[8] Y. Tan, Y. Kang, W. Wang, X. Lv, B. Wang, Q.i. Zhang, C. Cui, S. Cui, S. Jiao, G. Pang, S. Feng, Chitosan modified inorganic nanowires membranes for ultra-fast and efficient removal of Congo red, Appl. Surf. Sci. 569 (2021) 150970, https://doi.org/10.1016/j.apsusc.2021.150970.
[9] J. Liu, N. Wang, H. Zhang, J. Baeyens, Adsorption of Congo red dye on $Fe_xCo_{3-x}O_4$ nanoparticles, J. Environ. Manage. 238 (2019) 473–483.
[10] I.M. Alarifi, Y.O. Al-Ghamdi, R. Darwesh, M.O. Ansari, M.K. Uddin, Properties and application of MoS2 nanopowder: characterization Congo red dye adsorption, and optimization, J. Mater. Res. Technol. 13 (2021) 1169–1180.
[11] R. Ahmad, K. Ansari, Comparative study for adsorption of congo red and methylene blue dye on chitosan modified hybrid nanocomposite, Process Biochem. 108 (2021) 90–102.
[12] G. Ohemeng-Boahen, D.D. Sewu, H.N. Tran, S.H. Woo, Enhanced adsorption of congo red from aqueous solution using chitosan/hematite nanocomposite hydrogel capsule fabricated via anionic surfactant gelation, Colloids Surf., A 625 (2021) 126911, https://doi.org/10.1016/j.colsurfa.2021.126911.
[13] T. Taher, R. Putra, N. Rahayu Palapa, A. Lesbani, Preparation of magnetite-nanoparticle-decorated NiFe layered double hydroxide and its adsorption performance for congo red dye removal, Chem. Phys. Lett. 777 (2021) 138712, https://doi.org/10.1016/j.cplett.2021.138712.
[14] S. Al-Salihi, A.M. Jasim, M.M. Fidalgo, Y. Xing, Removal of Congo red dyes from aqueous solutions by porous γ-alumina nanoshells, Chemosphere 286 (2022) 131769, https://doi.org/10.1016/j.chemosphere.2021.131769.
[15] A. Dbik, S. Bentahar, M. El Khomri, N. El Messaoudi, A. Lacherai, Adsorption of Congo red dye from aqueous solutions using tunics of the corm of the saffron, Materialstoday: Proceedings 22 (1) (2021) 134–139.
[16] J. Tang, Y.-F. Zhang, Y. Liu, Y. Li, H. Hu, Efficient ion-enhanced adsorption of congo red on polyacrolein from aqueous solution: experiments, characterization and mechanism studies, Sep. Purif. Technol. 252 (2020) 117445, https://doi.org/10.1016/j.seppur.2020.117445.
[17] N. Chouikhi, J.A. Cecilia, E. Vilarrasa-García, L. Serrano-Cantador, S. Besghaier, M. Chlendi, M. Bagane, E.R. Castellón, Valorization of agricultural waste as a carbon materials for selective separation and storage of CO_2, H_2 and N_2, Biomass Bioenergy 155 (2021) 106297, https://doi.org/10.1016/j.biombioe.2021.106297.
[18] M. Lewoyehu, Comprehensive review on synthesis and application of activated carbon from agricultural residues for the remediation of venomous pollutants in wastewater, J. Anal. Appl. Pyrol. 159 (2021) 105279, https://doi.org/10.1016/j.jaap.2021.105279.
[19] J.O.P. Nayagam, K. Prasanna, Utilization of shell-based agricultural waste adsorbents for removing dyes: a review, Chemosphere 132737 (2021).
[20] M. Kamaraj, T.G. Nithya, S. Shyamalagowri, J. Aravind, R. Mythili, Activated carbon derived from almond tree dry leaves waste for enhanced multi dye removal from aqueous solutions, Mater. Lett. 308 (2022) 131216, https://doi.org/10.1016/j.matlet.2021.131216.
[21] C. Guclu, K. Alper, M. Erdem, K. Tekin, S. Karagoz, Activated carbons from co-carbonization of waste truck tires and spent tea leaves, Sustain. Chem. Pharm. 21 (2021) 100410, https://doi.org/10.1016/j.scp.2021.100410.
[22] S.K. Arumugasamy, G. Chellasamy, S. Sekar, S. Lee, S. Govindaraju, K. Yun, TriMOF synergized on the surface of activated carbon produced from pineapple leaves for the environmental pollutant reduction and oxygen evolution process, Chemosphere 286 (2022) 131893, https://doi.org/10.1016/j.chemosphere.2021.131893.
[23] P. Negi, A.K. Chhantyal, A.K. Dixit, S. Kumar, A. Kumar, Activated carbon derived from mango leaves as an enhanced microwave absorbing material, Sustain. Mater. Technol. 27 (2021) e00244.
[24] A.K. Tripathi, S. Murugavel, R.K. Singh, Dead Ashoka (*Saraca asoca*) leaves–derived porous activated carbons and flexible iongel polymer electrolyte for high-energy-density electric double-layer capacitors, Mater. Today Sustain. 11-12 (2021) 100062, https://doi.org/10.1016/j.mtsust.2021.100062.
[25] A.K. Prajapati, S. Das, M.K. Mondal, Exhaustive studies on toxic Cr(VI) removal mechanism from aqueous solution using activated carbon of *Aloe vera* waste leaves, J. Mol. Liq. 307 (2020) 112956, https://doi.org/10.1016/j.molliq.2020.112956.
[26] A.K. Mohamedkhair, M.A. Aziz, S.S. Shah, M.N. Shaikh, A.K. Jamil, M.A.A. Qasem, I.A. Buliyaminu, Z.H. Yamani, Effect of an activating agent on the physicochemical properties and supercapacitor performance of naturally

nitrogen-enriched carbon derived from *Albizia procera* leaves, Arabian J. Chem. 13 (7) (2020) 6161–6173.
[27] A.J. Veeraragavan, R. Shanmugavel, N. Abraham, D. Subramanian, S. Pandian, Kinetic studies validated by Artificial Neural Network simulation for the removal of dye from simulated waste water by the activated carbon produced from Acalypha indica leaves, Environ. Technol. Innovat. 21 (2021) 101244, https://doi.org/10.1016/j.eti.2020.101244.
[28] Jalab, J., Abdelwahed, W., Kitaz, A., Al-Kayali, R., 2021. Green synthesis of silver nanoparticles using aqueous extract of *Acacia cyanophylla* and its antibacterial activity, 7 (9), e08033.
[29] P. Das, T. Dutta, S. Manna, S. Loganathan, P. Basak, Facile green synthesis of non-genotoxic, non-hemolytic organometallic silver nanoparticles using extract of crushed, wasted, and spent *Humulus lupulus (hops)*: Characterization, anti-bacterial, and anti-cancer studies, Environ. Res. 204 (2022) 111962, https://doi.org/10.1016/j.envres.2021.111962.
[30] M. Sarkar, S. Denrah, M. Das, M. Das, Statistical optimization of bio-mediated silver nanoparticles synthesis for use in catalytic degradation of some azo dyes, Chem. Phys. Impact 3 (2021) 100053, https://doi.org/10.1016/j.chphi.2021.100053.
[31] M.A. Yassin, A.M. Elgorban, A.-E.-R.-M.-A. El-Samawaty, B.M.A. Almunqedhi, Biosynthesis of silver nanoparticles using *Penicillium verrucosum* and analysis of their antifungal activity, Saudi J. Biol. Sci. 28 (4) (2021) 2123–2127.
[32] P. Rani, L. Trivedi, S.S. Gaurav, A. Singh, G. Shukla, Green synthesis of silver nanoparticles by *Cassytha filiformis L.* extract and its characterization, Materialstoday: Proceedings 49 (2022) 3510–3516, https://doi.org/10.1016/j.matpr.2021.07.166.
[33] M.P. Patil, Y.-A. Seong, J.-O. Kim, Y.B. Seo, G.-D. Kim, Synthesis of silver nanoparticles using aqueous extract of Cuscuta japonica seeds and their antibacterial and antioxidant activities, Inorg. Chem. Commun. 134 (2021) 109035, https://doi.org/10.1016/j.inoche.2021.109035.
[34] N. Korkmaz, Y. Ceylan, A. Hamid, A. Karadağ, A.S. Bülbül, M.N. Aftab, Ö. Çevik, F. Şen, Biogenic silver nanoparticles synthesized via Mimusops elengi fruit extract, a study on antibiofilm, antibacterial, and anticancer activities, J. Drug Delivery Sci. Technol. 59 (2020) 101864, https://doi.org/10.1016/j.jddst.2020.101864.
[35] G. Zhang, R. Zhang, F. Wang, Fast formation kinetics of methane hydrates loaded by silver nanoparticle coated activated carbon (Ag-NP@AC), Chem. Eng. J. 417 (2021) 129206, https://doi.org/10.1016/j.cej.2021.129206.
[36] A. Mishra, N.K. Kaushik, M. Sardar, D. Sahal, Evaluation of antiplasmodial activity of green synthesized silver nanoparticles, Colloids Surf., B 111 (2013) 713–718.
[37] M.N. Owaid, M.A. Rabeea, A. Abdul Aziz, M.S. Jameel, M.A. Dheyab, Mycogenic fabrication of silver nanoparticles using Picoa, Pezizales, characterization and their antifungal activity, Environ. Nanotechnol. Monit. Manage. 17 (2022) 100612, https://doi.org/10.1016/j.enmm.2021.100612.
[38] M.M. El-Sheekh, L.H.S. Hassan, H.H. Morsi, Assessment of the in vitro anticancer activities of cyanobacteria mediated silver oxide and gold nanoparticles in human colon CaCo-2 and cervical HeLa cells, Environ. Nanotechnol. Monit. Manage. 16 (2021) 100556, https://doi.org/10.1016/j.enmm.2021.100556.
[39] M.P. Moisés, C.T. P. da Silva, C.A.A. Silva, J.G. Meneguin, G.G. Fonseca, M.R. Guilherme, A.W. Rinaldi, E.M. Girotto, E. Radovanovic, Preparation of a sustainable Zeolite A using an agroindustry solid waste loaded with silver nanoparticles: antimicrobial activity study, Mater. Lett. 308 (2022) 131194, https://doi.org/10.1016/j.matlet.2021.131194.
[40] A. Kavitha, S. Shanmugan, C.G. Awuchi, C. Kanagaraj, S. Ravichandran, Synthesis and enhanced antibacterial using plant extracts with silver nanoparticles: therapeutic application, Inorg. Chem. Commun. 134 (2021) 109045, https://doi.org/10.1016/j.inoche.2021.109045.
[41] Melkamu, W.W., Bitew, L.T., 2021. Green synthesis of silver nanoparticles using *Hagenia abyssinica* (Bruce) J.F. Gmel plant leaf extract and their antibacterial and anti-oxidant activities, Heliyon, e08459.
[42] M. Oves, M. Ahmar Rauf, M. Aslam, H.A. Qari, H. Sonbol, I. Ahmad, G. Sarwar Zaman, M. Saeed, Green synthesis of silver nanoparticles by *Conocarpus lancifolius* plant extract and their antimicrobial and anticancer activities, Saudi J. Biol. Sci. 29 (1) (2022) 460–471, https://doi.org/10.1016/j.sjbs.2021.09.007.
[43] T.A. Salih, K.T. Hassan, S.R. Majeed, I.J. Ibraheem, O.M. Hassan, A.S. Obaid, In vitro scolicidal activity of synthesised silver nanoparticles from aqueous plant extract against *Echinococcus granulosus*, Biotechnol. Rep. 28 (2020) e00545.
[44] C. Pragathiswaran, J. Violetmary, A. Faritha, K. Selvarani, P. MohideenAskar Nawas, Photocatalytic degradation, sensing of Cd^{2+} using silver nanoparticles synthesised from plant extract of *cissus quadrangularis* and their microbial activity, Mater. Today: Proc. 45 (2021) 3348–3356.
[45] K. Chandhirasekar, A. Thendralmanikandan, P. Thangavelu, B.-S. Nguyen, T.-A. Nguyen, K. Sivashanmugan, A. Nareshkumar, V.-H. Nguyen, Plant-extract-assisted green synthesis and its larvicidal activities of silver nanoparticles using leaf extract of *Citrus medica, Tagetes lemmonii,* and *Tarenna asiatica*, Mater. Lett. 287 (2021) 129265, https://doi.org/10.1016/j.matlet.2020.129265.
[46] E.K. Kambale, C.I. Nkanga, B.-P. Mutonkole, A.M. Bapolisi, D.O. Tassa, J.-M. Liesse, R.W.M. Krause, P.B. Memvanga, Green synthesis of antimicrobial silver nanoparticles using aqueous leaf extracts from three Congolese plant species (*Brillantaisia patula, Crossopteryx febrifuga* **and** *Senna siamea*), Heliyon 6 (8) (2020) e04493, https://doi.org/10.1016/j.heliyon.2020.e04493.
[47] G. Sharma, T.S. AlGarni, P.S. Kumar, S. Bhogal, A. Kumar, S. Sharma, M.u. Naushad, Z.A. ALOthman, F.J. Stadler, Utilization of Ag_2O–Al_2O_3–ZrO_2 decorated onto rGO as adsorbent for the removal of Congo red from aqueous solution, 2021, Environ. Res. 197 (2021) 111179, https://doi.org/10.1016/j.envres.2021.111179.
[48] A.O. Basheer, M.M. Hanafiah, M.A. Alsaadi, Y. Al-Douri, A.A. Al-Raad, Synthesis and optimization of high surface area mesoporous date palm fiber-based nanostructured powder activated carbon for aluminum removal, Chin. J. Chem. Eng. 32 (2021) 472–484.
[49] N. Abbasi, S.A. Khan, T.A. Khan, Response surface methodology mediated process optimization of Celestine blue B uptake by novel custard apple seeds activated carbon/$FeMoO_4$ nanocomposite, J. Water Process Eng. 43 (2021) 102267, https://doi.org/10.1016/j.jwpe.2021.102267.
[50] K.-W. Jung, B.H. Choi, K.G. Song, J.-W. Choi, Statistical optimization of preparing marine macroalgae derived activated carbon/iron oxide magnetic composites for sequestering acetylsalicylic acid from aqueous media using response surface Methodologys, Chemosphere 215 (2019) 432–443.
[51] B. Sadhukhan, N.K. Mondal, S. Chattoraj, Optimization using central composite design (CCD) and the desirability function for sorption of methylene blue from aqueous solution onto Lemna major, Karbala Int. J. Mod. Sci. 2 (2016) 145–155.
[52] I.Y. Mohammed, Y.A. Abakr, S. Yusup, F.K. Kazi, Valorization of Napier grass via intermediate pyrolysis: optimization using response surface methodology and pyrolysis products characterization, J. Cleaner Prod. 142 (2017) 1848–1866.
[53] K.C. Bedin, A.L. Cazetta, I.P.A.F. Souza, O. Pezoti, L.S. Souza, P.S.C. Souza, J.T.C. Yokoyama, V.C. Almeida, Porosity enhancement of spherical activated carbon: Influence and optimization of hydrothermal synthesis conditions using response surface methodology, J. Environ. Chem. Eng. 6 (1) (2018) 991–999.
[54] M. Auta, B.H. Hameed, Optimized waste tea activated carbon for adsorption of Methylene Blue and Acid Blue 29 dyes using response surface methodology, Chem. Eng. J. 175 (2011) 233–243.
[55] S.K. Theydan, M.J. Ahmed, Optimization of preparation conditions for activated carbons from date stones using response surface methodology, Powder Technol. 224 (2012) 101–108.
[56] D. Awotwe-Otoo, C. Agarabi, P.J. Faustino, M.J. Habib, S. Lee, M.A. Khan, R.B. Shah, Application of quality by design elements for the development and optimization of an analytical method for protamine sulfate, J. Pharm. Biomed. Anal. 62 (2012) 61–67.
[57] F. Al-Otibi, K. Perveen, N.A. Al-Saif, R.I. Alharbi, N.A. Bokhari, G. Albasher, R.M. Al-Otaibi, M.A. Al-Mosa, Biosynthesis of silver nanoparticles using Malva parviflora and their antifungal activity, Saudi J. Biol. Sci. 28 (4) (2021) 2229–2235.
[58] M. Narayanan, S. Divya, D. Natarajan, S. Senthil-Nathan, S. Kandasamy, A. Chinnathambi, T.A. Alahmadi, A. Pugazhendhi, Green synthesis of silver nanoparticles from aqueous extract of *Ctenolepis garcini L.* and assess their possible biological applications, Process Biochem. 107 (2021) 91–99.
[59] M. Kamaraj, N.R. Srinivasan, G. Assefa, A.T. Adugna, M. Kebede, Facile development of sunlit ZnO nanoparticles-activated carbon hybrid from pernicious weed as an operative nano-adsorbent for removal of methylene blue and chromium from aqueous solution: extended application in tannery industrial wastewater, Environ. Technol. Innovation 17 (2020) 100540, https://doi.org/10.1016/j.eti.2019.100540.
[60] P. Sudhakar, H. Soni, Catalytic reduction of Nitrophenols using silver nanoparticles-supported activated carbon derived from agro-waste, J. Environ. Chem. Eng. 6 (2018) 28–36.
[61] S. Mandal, J. Calderon, S.B. Marpu, M.A. Omary, S.Q. Shi, Mesoporous activated carbon as a green adsorbent for the removal of heavy metals and Congo red: characterization, adsorption kinetics, and isotherm studies, J. Contam. Hydrol. 243 (2021) 103869, https://doi.org/10.1016/j.jconhyd.2021.103869.
[62] M.A. Hegazy, M.M. Mohammedy, A.S. Dhmees, Phosphorous and sulfur doped asphaltene derived activated carbon for supercapacitor application, J. Storage Mater. 44 (2021) 103331, https://doi.org/10.1016/j.est.2021.103331.
[63] A. Ghahremani, M. Manteghian, H. Kazemzadeh, Removing lead from aqueous solution by activated carbon nanoparticle impregnated on lightweight expanded clay aggregate, J. Environ. Chem. Eng. 9 (1) (2021) 104478, https://doi.org/10.1016/j.jece:2020.104478.
[64] G.A. Filip, A. Florea, D. Olteanu, S. Clichici, L. David, B. Moldovan, M. Cenariu, I. Scrobota, M. Potara, I. Baldea, Biosynthesis of silver nanoparticles using *Sambucus nigra L.* fruit extract for targeting cell death in oral dysplastic cells, Mater. Sci. Eng. C 123 (2021) 111974, https://doi.org/10.1016/j.msec.2021.111974.
[65] N. Zamanpour, A. Mohammad Esmaeily, M. Mashreghi, B. Shahnavaz, M. Reza Sharifmoghadam, A. Kompany, Application of a marine luminescent Vibrio sp. B4L for biosynthesis of silver nanoparticles with unique characteristics, biochemical properties, antibacterial and antibiofilm activities, Bioorg. Chem. 114 (2021) 105102, https://doi.org/10.1016/j.bioorg.2021.105102.
[66] Taha, A., Aissa, M. B., Da'na, E., 2020. Green Synthesis of an Activated Carbon-Supported Ag and ZnO Nanocomposite for Photocatalytic Degradation and Its Antibacterial Activities, Molecules, 25, 1586.
[67] M.D. Yahya, I. Yohanna, M. Auta, K.S. Obayomi, Remediation of Pb (II) ions from Kagara gold mining effluent using cotton hull adsorbent, Scientific African 8 (2020) e00399, https://doi.org/10.1016/j.sciaf.2020.e00399.
[68] S.-L. Bee, Y. Bustami, A. Ul-Hamid, Z.A.A. Hamid, Green biosynthesis of hydroxyapatite-silver nanoparticle nanocomposite using aqueous Indian

curry leaf (Murraya koengii) extract and its biological properties, Mater. Chem. Phys. 277 (2022) 125455, https://doi.org/10.1016/j.matchemphys.2021.125455.
[69] F. Kiani Ghaleh sardi, M. Behpour, Z. Ramezani, S. Masoum, Simultaneous removal of Basic Blue41 and Basic Red46 dyes in binary aqueous systems via activated carbon from palm bio-waste: Optimization by central composite design, equilibrium, kinetic, and thermodynamic studies, Environ. Technol. Innovat. 24 (2021) 102039, https://doi.org/10.1016/j.eti.2021.102039.
[70] B. Liu, C. Du, J.J. Chen, J.Y. Zhai, Y. Wang, H.L. Li, Preparation of well-developed mesoporous activated carbon fibers from plant pulp fibers and its adsorption of methylene blue from solution, Chem. Phys. Lett. 771 (2021) 138535, https://doi.org/10.1016/j.cplett.2021.138535.
[71] Y. Ji, F. Xu, W. Wei, H. Gao, K. Zhang, G. Zhang, Y. Xu, P. Zhang, Efficient and fast adsorption of methylene blue dye onto a nanosheet MFI zeolite, J. Solid State Chem. 295 (2021) 121917, https://doi.org/10.1016/j.jssc.2020.121917.
[72] B. Zhu, P. Xia, W. Ho, J. Yu, Isoelectric point and adsorption activity of porous g-C_3N_4, Appl. Surf. Sci. 344 (2015) 188–195.
[73] M. Qu, W. Yao, X. Cui, R. Xia, L.i. Qin, X. Liu, Biosynthesis of silver nanoparticles (AgNPs) employing Trichoderma strains to control empty-gut disease of oak silkworm (Antheraea pernyi), Mater. Today Commun. 28 (2021) 102619, https://doi.org/10.1016/j.mtcomm.2021.102619.
[74] R. Lafi, I. Montasser, A. Hafiane, Adsorption of Congo red dye from aqueous solutions by prepared activated carbon with oxygen-containing functional groups and its regeneration, Adsorpt. Sci. Technol. 37 (1-2) (2019) 160–181.
[75] Q.-u.-A. Qurrat-ul-Ain, S. Khurshid, Z. Gul, J. Khatoon, M.R. Shah, I. Hamid, I.A. T. Khan, F. Aslam, Anionic azo dyes removal from water using amine-functionalized cobalt–iron oxide nanoparticles: a comparative time-dependent study and structural optimization towards the removal mechanism, RSC Adv. 10 (2) (2020) 1021–1041.
[76] J.N. Edokpayi, E. Makete, Removal of Congo red dye from aqueous media using Litchi seeds powder: equilibrium, kinetics and thermodynamics, Phys. Chem. Earth Parts A/B/C 123 (2021) 103007, https://doi.org/10.1016/j.pce:2021.103007.
[77] K.-H. Wu, W.-C. Huang, W.-C. Hung, C.-W. Tsai, Modified expanded graphite/Fe_3O_4 composite as an adsorbent of methylene blue: adsorption kinetics and isotherms, Mater. Sci. Eng., B 266 (2021) 115068, https://doi.org/10.1016/j.mseb.2021.115068.
[78] S.D.K. Seera, D. Kundu, P. Gami, P.K. Naik, T. Banerjee, Synthesis and characterization of xylan-gelatin cross-linked reusable hydrogel for the adsorption of methylene blue, Carbohydr. Polym. 256 (2021) 117520.
[79] M.K. Habibi, S.M. Rafiaei, A. Alhaji, M. Zare, Synthesis of $ZnFe_2O_4$: 1 wt% Ce^{3+}/Carbon fibers composite and investigation of its adsorption characteristic to remove Congo red dye from aqueous solutions, J. Alloy. Compd. 890 (2021) 161901.
[80] H. Ouassif, E.M. Moujahid, R. Lahkale, R. Sadik, F.Z. Bouragba, E.M. Sabbar, M. Diouri, Zinc-Aluminum layered double hydroxide: high efficient removal by adsorption of tartrazine dye from aqueous solution, Surf. Interfaces 18 (2020) 100401, https://doi.org/10.1016/j.surfin.2019.100401.
[81] N. Kataria, V.K. Garg, Removal of Congo red and Brilliant green dyes from aqueous solution using flower shaped ZnO nanoparticles, J. Environ. Chem. Eng. 5 (6) (2017) 5420–5428.
[82] I. Amar, A. Sharif, M. Ali, S. Alshareef, F. Altohami, M. Abdulqadir, M.M. Ahwidi, Removal of methylene blue from aqueous solutions using nano-magnetic adsorbent based on zinc-doped cobalt ferrite, Chem. Methodol. 4 (2020) 1–18.
[83] I. Langmuir, The constitution and fundamental properties of solids and liquids, J. Am. Chem. Soc. 38 (11) (1916) 2221–2295.
[84] H.M.F. Freundlich, Over the adsorption in solution, J. Phys. Chem. 57 (1906) 385–471.
[85] M.I. Tempkin, V. Pyzhev, Kinetics of ammonia synthesis on promoted iron catalyst, Acta physicochimica URSS 12 (1904) 327–356.
[86] Dubinin, M.M., Radushkevich, L.V., 1947. The equation of the characteristic curve of the activated charcoal, Proceedings of the Academy of Sciences of the USSR, Physical Chemistry section, 55, 331–337.
[87] Y. Feng, H. Wang, J. Xu, X. Du, X.u. Cheng, Z. Du, H. Wang, Fabrication of MXene/PEI functionalized sodium alginate aerogel and its excellent adsorption behavior for Cr(VI) and Congo Red from aqueous solution, J. Hazard. Mater. 416 (2021) 125777, https://doi.org/10.1016/j.jhazmat.2021.125777.
[88] M.A. Salam, R.M. El-Shishtawy, A.Y. Obaid, Synthesis of magnetic multi-walled carbon nanotubes/magnetite/ chitin magnetic nanocomposite for the removal of Rose Bengal from real and model solution, J. Ind. Eng. Chem. 20 (5) (2014) 3559–3567.
[89] K.S. Obayomi, J.O. Bello, M.D. Yahya, E. Chukwunedum, J.B. Adeoye, Statistical analyses on effective removal of cadmium and hexavalent chromium ions by multiwall carbon nanotubes (MWCNTs), Heliyon 6 (6) (2020) e04174, https://doi.org/10.1016/j.heliyon.2020.e04174.
[90] F. Amran, M.A.A. Zaini, Sodium hydroxide-activated Casuarina empty fruit: isotherm, kinetics and thermodynamics of methylene blue and congo red adsorption, Environ. Technol. Innovation 23 (2021) 101727, https://doi.org/10.1016/j.eti.2021.101727.
[91] S. Wei, A.R. Kamali, Waste plastic derived Co_3Fe_7/$CoFe_2O_4$@carbon magnetic nanostructures for efficient dye adsorption, J. Alloy. Compd. 886 (2021) 161201, https://doi.org/10.1016/j.jallcom.2021.161201.
[92] QinQin, M. Li, P. Lan, Y. Liao, S. Sun, H. Liu, Novel $CaCO_3$/chitin aerogel: Synthesis and adsorption performance toward Congo red in aqueous solutions, Int. J. Biol. Macromol. 181 (2021) 786–792.
[93] M.M.H. El-Sayed, R.E. Elsayed, A. Attia, H.H. Farghal, R.A. Azzam, T.M. Madkour, Novel nanoporous membranes of bio-based cellulose acetate, poly(lactic acid) and biodegradable polyurethane in-situ impregnated with catalytic cobalt nanoparticles for the removal of Methylene Blue and Congo Red dyes from wastewater, Carbohydrate Polym. Technol. Appl. 2 (2021) 100123, https://doi.org/10.1016/j.carpta.2021.100123.
[94] S.G. Mohammad, M.M.H. El-Sayed, Removal of imidacloprid pesticide using nanoporous activated carbons produced via pyrolysis of peach stone agricultural wastes, Chem. Eng. Commun. 208 (8) (2021) 1069–1080.
[95] Y. Pi, C. Duan, Y. Zhou, S. Sun, Z. Yin, H. Zhang, C. Liu, Y.e. Zhao, The effective removal of Congo red using a bio-nanocluster: Fe_3O_4 nanoclusters modified bacteria, J. Hazard. Mater. 424 (2022) 127577, https://doi.org/10.1016/j.jhazmat.2021.127577.
[96] T.A. Saleh, Isotherm, kinetic, and thermodynamic studies on Hg(II) adsorption from aqueous solution by silica- multiwall carbon nanotubes, Environ. Sci. Pollut. Res. 22 (21) (2015) 16721–16731.
[97] P. Debnath, N.K. Mondal, Effective removal of congo red dye from aqueous solution using biosynthesized zinc oxide nanoparticles, Environ. Nanotechnol. Monit. Manage. 14 (2020) 100320, https://doi.org/10.1016/j.enmm.2020.100320.
[98] H.J. Gao, S.F. Wang, L.M. Fang, G.A. Sun, X.P. Chen, S.N. Tang, H. Yang, G.Z. Sun, D.E. Li, Nanostructured spinel-type M(M = Mg Co, Zn)Cr2O4 oxides: novel adsorbents for aqueous Congo red removal, Mater. Today Chem. 22 (2021) 100593.
[99] W.A. Shaikh, R.U. Islam, S. Chakraborty, Stable silver nanoparticle doped mesoporous biochar-based nanocomposite for efficient removal of toxic dyes, J. Environ. Chem. Eng. 9 (1) (2021) 104982, https://doi.org/10.1016/j.jece:2020.104982.
[100] R. Ozola-Davidane, J. Burlakovs, T. Tamm, S. Zeltkalne, A.E. Krauklis, M. Klavins, Bentonite-ionic liquid composites for Congo red removal from aqueous solutions, J. Mol. Liq. 337 (2021) 116373, https://doi.org/10.1016/j.molliq.2021.116373.
[101] J. Iqbal, N.S. Shah, M. Sayed, N.K. Niazi, M. Imran, J.A. Khan, Z.U.H. Khan, A.G.S. Hussien, K. Polychronopoulou, F. Howari, Nano-zerovalent manganese/biochar composite for the adsorptive and oxidative removal of Congo-red dye from aqueous solutions, J. Hazard. Mater. 403 (2021) 123854, https://doi.org/10.1016/j.jhazmat.2020.123854.
[102] C. Arab, R. El Kurdi, D. Patra, Efficient removal of Congo red using curcumin conjugated zinc oxide nanoparticles as new adsorbent complex, Chemosphere 276 (2021) 130158, https://doi.org/10.1016/j.chemosphere.2021.130158.
[103] Y.S. Ho, G. McKay, Pseudo-second order model for sorption processes, Process Biochem. 34 (5) (1999) 451–465.
[104] W.J. Weber, J.C. Morris, Kinetics of adsorption on carbon from solution, J. Sanitary Eng Div. Proceed. Am. Soc. Civil. Eng. 89 (2) (1963) 31–59.
[105] G.E. Boyd, A.W. Adamson, L.S. Myers, The exchange adsorption of ions from aqueous solutions by organic zeolites II kinetics, J. Am. Chem. Soc. 69 (1947) 2836–2848.
[106] V. Sri Devi, B. Sudhakar, K. Prasad, P. Jeremiah Sunadh, M. Krishna, Adsorption of Congo red from aqueous solution onto Antigonon leptopus leaf powder: Equilibrium and kinetic modeling, Mater. Today:. Proc. 26 (2020) 3197–3206, https://doi.org/10.1016/j.matpr.2020.02.715.
[107] S. Lagergren, B.K. Svenska, On the theory of so-called adsorption of dissolved substances, Roy. Swedish Acad. Sci. Doc. 24 (1898) 1–13.